

X-Shooter spectroscopy of young stellar objects:

IV – Accretion in low-mass stars and sub-stellar objects in Lupus ^{*,**}

J.M. Alcalá¹, A. Natta^{2,9}, C.F. Manara⁷, L. Spezzi⁷, B. Stelzer³, A. Frasca⁴, K. Biazzo^{4,1}, E. Covino¹,
S. Randich², E. Rigliaco⁸, L. Testi^{2,7,11}, F. Comerón⁷, G. Cupani⁵, and V. D’Elia^{6,10}

¹ INAF-Osservatorio Astronomico di Capodimonte, via Moiariello 16, I-80131 Napoli, Italy

² INAF-Osservatorio Astrofisico di Arcetri, via Moiariello 16, Largo E. Fermi 5, I-50125 Firenze, Italy

³ INAF-Osservatorio Astronomico di Palermo, Piazza del Parlamento 1, I-90134 Palermo, Italy

⁴ INAF-Osservatorio Astrofisico di Catania, via S. Sofia 78, I-95123 Catania, Italy

⁵ INAF-Osservatorio Astronomico di Trieste, via Tiepolo 11, 34143 Trieste, Italy

⁶ INAF-Osservatorio Astronomico di Roma, Via Frascati 33, I-00040 Monteporzio Catone, Italy

⁷ European Southern Observatory, Karl Schwarzschild Str. 2, 85748 Garching, Germany

⁸ Department of Planetary Science, Lunar and Planetary Lab. University of Arizona, 1629, E. University Blvd, 85719, Tucson, AZ, USA

⁹ DIAS/Dublin Institute for Advanced Studies, Burlington Road, Dublin 4, Ireland

¹⁰ ASI-Science Data Centre, Via Galileo Galilei, I-00044 Frascati, Italy

¹¹ Excellence Cluster Universe, Boltzmannstr. 2, D-85748 Garching, Germany

Received July, 7th 2013 ; accepted October, 3rd 2013

ABSTRACT

We present X-Shooter/VLT observations of a sample of 36 accreting low-mass stellar and sub-stellar objects (YSOs) in the Lupus star forming region, spanning a range in mass from ~ 0.03 to $\sim 1.2 M_{\odot}$, but mostly with $0.1 M_{\odot} < M_{\star} < 0.5 M_{\odot}$. Our aim is twofold: firstly, analyse the relationship between excess-continuum and line emission accretion diagnostics, and, secondly, to investigate the accretion properties in terms of the physical properties of the central object. The accretion luminosity (L_{acc}), and from it the accretion rate (\dot{M}_{acc}), is derived by modelling the excess emission, from the UV to the near-IR, as the continuum emission of a slab of hydrogen. The flux and luminosity (L_{line}) of a large number of emission lines of H, He, Ca II, etc., observed simultaneously in the range from ~ 330 nm to 2500 nm, were computed. The luminosity of all the lines is well correlated with L_{acc} . We provide empirical relationships between L_{acc} and the luminosity of 39 emission lines, which have a lower dispersion as compared to previous relationships in the literature. Our measurements extend the Pa β and Br γ relationships to L_{acc} values about two orders of magnitude lower than those reported in previous studies. We confirm that different methodologies to measure L_{acc} and \dot{M}_{acc} yield significantly different results: H α line profile modelling may underestimate \dot{M}_{acc} by 0.6 to 0.8 dex with respect to \dot{M}_{acc} derived from continuum-excess measures. Such differences may explain the likely spurious bi-modal relationships between \dot{M}_{acc} and other YSOs properties reported in the literature. We derive \dot{M}_{acc} in the range $2 \times 10^{-12} - 4 \times 10^{-8} M_{\odot} \text{ yr}^{-1}$ and conclude that $\dot{M}_{\text{acc}} \propto M_{\star}^{1.8(\pm 0.2)}$, with a dispersion lower by a factor of about 2 than in previous studies. A number of properties indicate that the physical conditions of the accreting gas are similar over more than 5 orders of magnitude in \dot{M}_{acc} , confirming previous suggestions that it is the geometry of the accretion flow that controls the rate at which the disc material accretes onto the central star.

Key words. Stars: pre-main sequence, low-mass – Accretion, accretion disks – Line: formation, identification – Open clusters and associations: Lupus

1. Introduction

The mass accretion rate is a key quantity for the studies of pre-main sequence (PMS) stellar evolution. The evolution of accretion discs around young low-mass ($M_{\star} < 0.5 M_{\odot}$) stellar and sub-stellar objects (YSOs) is regulated by the simultaneous effects of the mass accretion onto the star and

the ejection of matter from the star-disc system (Patz & Camenzind 1996, and references therein). Understanding the evolution of accretion discs can provide strong constraints on theories of planet formation and evolution. The mass accretion rate, \dot{M}_{acc} , sets an important constraint for the disc evolution models (Hartmann et al. 1998) and disc clearing mechanisms (Alexander et al. 2006; Gorti & Hollenbach 2009).

All young objects, from intermediate mass stars to brown dwarfs, show at some stage of their evolution evidence of circumstellar discs and accretion. The currently accepted paradigm that explains mass accretion in YSOs is the magnetospheric accretion model (Uchida & Shibata 1985; Königl 1991; Shu et al. 1994). The model assumes

Send offprint requests to: J.M. Alcalá

* Based on observations collected at the European Southern Observatory at Paranal, under programs 084.C-0269(A), 085.C-0238(A), 086.C-0173(A), 087.C-0244(A) and 089.C-0143(A).

** The on-line material Figures C.1 to C.10 and Tables C.1 to C.11, are available only in electronic form.

Correspondence to: alcalá@oacn.inaf.it

that matter from the inner edge of the accretion disc is channelled along the magnetic field lines onto the star. The gas shocking at the stellar surface produces high temperatures ($\sim 10^4$ K), giving rise to continuum and line emission in the accretion flows. Balmer continuum radiation is mostly emitted in the optically thin pre-shock gas, while Paschen continuum emission is generally produced in optically thick post-shock gas. Emission in the Balmer lines as well as in other lines of Ca II and He I originates mainly in the accretion columns (Hartmann et al. 1994; Calvet & Gullbring 1998; Muzerolle et al. 2001; Kurosawa et al. 2006). The accretion luminosity, L_{acc} , which measures the radiative losses, integrated over the whole spectrum, can be converted into mass accretion rate, \dot{M}_{acc} , if the YSOs radius and mass are known (Gullbring et al. 1998; Hartmann 1998).

In the past, L_{acc} has been calculated using veiling measurements in high-resolution spectra (e.g. Hartigan et al. 1991; Hartigan & Kenyon 2003; White & Hillenbrand 2004, and references therein), or by modelling the Balmer and Paschen continuum excess emission with a plane-parallel slab of hydrogen in local thermodynamic equilibrium (LTE) (e.g. Valenti et al. 1993; Gullbring et al. 1998; Herczeg & Hillenbrand 2008; Rigliaco et al. 2012). More recently, the continuum excess emission has been measured by incorporating in the models multiple accretion components with a large range of energy fluxes (Ingleby et al. 2013).

First direct measurements of UV excess emission in very low-mass stars and sub-stellar objects were done by Herczeg & Hillenbrand (2008); Herczeg et al. (2009) and Rigliaco et al. (2012). Prior to these studies, the difficulty of detecting the Balmer continuum emission in brown dwarfs called for the necessity of developing magnetospheric accretion models to reproduce the H α line profile (Muzerolle et al. 2001, 2003, 2005), more easily measured in these objects. These studies additionally showed that the size of the accretion flows and the mass accretion rate are correlated, suggesting that it is the geometry of the accretion flows that controls the rate at which the disc material accretes onto the central star (Muzerolle et al. 2001).

It has been shown that L_{acc} , hence \dot{M}_{acc} is well correlated with the line luminosity, L_{line} , of several emission lines of the Balmer series, He I and Ca II lines (e.g. Herczeg & Hillenbrand 2008; Rigliaco et al. 2012, and references therein), as well as with hydrogen recombination lines in the near infrared (Muzerolle et al. 1998; Calvet et al. 2004). This underlines the importance of these emission features as accretion diagnostics. The $\dot{M}_{\text{acc}}-L_{\text{line}}$ relationships were then extended down to the sub-stellar regime (Natta et al. 2004; Mohanty et al. 2005; Herczeg & Hillenbrand 2008), by combining measures of \dot{M}_{acc} using different methodologies for different mass regimes (spectral veiling determination and modelling of the H α line profile for the stars with M_{\star} greater and lower than $0.3M_{\odot}$, respectively). A two-mode relation, with respect to YSO mass, between \dot{M}_{acc} and the surface flux of the Ca II infrared triplet (IRT) line at 866.2 nm was suggested (Mohanty et al. 2005), but the origin of the bi-modality was unclear. A relationship between \dot{M}_{acc} and the width of the H α line at 10% of the line peak was also established, though with a large scatter (Natta et al. 2004).

Researchers have been using emission lines as proxies to measure L_{acc} (Muzerolle et al. 1998, 2000, 2001, 2005;

Natta et al. 2004; Mohanty et al. 2005; Gatti et al. 2006; Gatti et al. 2008; Antonucci et al. 2011; Biazzo et al. 2012, and references therein). When applied to large samples of YSOs, the $L_{\text{acc}}-L_{\text{line}}$ relations provided a correlation between accretion rate and mass of the central object, i.e. $\dot{M}_{\text{acc}} \propto M_{\star}^{\alpha}$ with $\alpha \approx 2$ (Muzerolle et al. 2005; Natta et al. 2006), but with a scatter of more than 2 dex in $\log \dot{M}_{\text{acc}}$, at a given YSO mass. Such a large scatter is not easily explained in terms of YSO variability (Costigan et al. 2012, 2013) or different methodological approach used to derive L_{acc} (Herczeg & Hillenbrand 2008).

The main caveat of the $L_{\text{acc}}-L_{\text{line}}$ relations is the non-simultaneity of photometry and spectral line measurements, complicated by the fact that emission lines can trace strong winds as well as mass accretion. Additionally, emission lines are produced not only by accretion, but also in other processes such as chromospheric activity. This adds more uncertainty on the L_{acc} determinations from lines. The uncertainty depends on the level of the accretion rate and on the stellar properties (see Manara et al. 2013a).

Deriving precise $L_{\text{acc}}-L_{\text{line}}$ relations for accretion requires well-calibrated observations of both the continuum and line fluxes over a wide range of wavelengths, and over the widest possible range of YSO physical parameters, i.e., L_{acc} , \dot{M}_{acc} , and M_{\star} . Furthermore, an accurate knowledge of both the photospheric and chromospheric spectrum of the YSO, which need to be subtracted from the observed flux to isolate the accretion emission, is required. On the other hand, a large number of emission line diagnostics over a wide wavelength need to be studied simultaneously to avoid problems related to YSO variability, in order to probe gas at different excitation conditions. These requirements can be fulfilled with the use of broad spectral range spectrographs such as X-Shooter (Vernet et al. 2011) at the VLT. X-shooter is an ideal instrument for this purpose, as its wide wavelength range (300-2500 nm), covered in a single shot, allows comparing many different accretion diagnostics simultaneously.

In this paper we present the analysis and results of X-Shooter observations of a sample of 36 accreting YSOs in the Lupus star forming region, spanning a range in mass from ~ 0.03 to $1.2 M_{\odot}$, but the majority with $M_{\star} < 0.5 M_{\odot}$. We use the continuum UV-excess emission as a measure of L_{acc} , hence of \dot{M}_{acc} , and provide revised relationships between L_{acc} and the luminosity, L_{line} , of an unprecedentedly large number of emission lines. The accretion properties of the sample are also analysed.

The sample and observations are presented in Section 2, while in Section 3 the sample characterisation is provided. The determinations of L_{acc} , obtained by fitting the Balmer and Paschen continua with a model of a slab of hydrogen, and derivation of \dot{M}_{acc} , as well as the luminosity of a number of permitted emission lines are presented in Section 4. The relationships between L_{acc} and L_{line} are derived in Section 5, while the accretion properties of the sample are examined in Section 6. The results are then discussed in Sections 7 and our main conclusions are summarised in Section 8.

2. Sample, observations and data reduction

As part of the consortium that built X-Shooter, INAF was granted 46 nights of guaranteed time observations (GTO) at the VLT-UT2 (Kueyen) spread over a period of three years, starting on ESO period 84. Eight of these nights were devoted to young stellar objects in nearby star forming regions (~ 3 , 3 and 2, nights for the σ -Ori cluster, the Lupus clouds and the TW Hya association, respectively). The data used in this paper were acquired within the context of the X-Shooter INAF/GTO (Alcalá et al. 2011) in April 06/07, 2010, April 23, 2011 and April 18, 2012.

2.1. The sample

We selected YSOs in the Lupus star forming region. The Lupus cloud complex is one of the low-mass star forming regions located closest ($d < 200$ pc) to the Sun (see Comerón 2008, for a review). Similarly to other regions (e.g., Taurus, Chamaeleon, and ρ -Oph), a large variety of objects in various stages of evolution are present in Lupus. Several sub-stellar objects have also been discovered in the region (Comerón 2008; López-Martí et al. 2003).

Our sample comprises 36 YSOs mainly in the Lupus I and III clouds satisfying as close as possible the following criteria: i) YSOs with infrared Class-II characteristics and low extinction to take full advantage of the broad X-Shooter spectral range, from UV to near-IR; ii) targets well surveyed in as many photometric bands as possible: mainly Spitzer (IRAC & MIPS) surveys and complementary Wide-field Infrared Survey Explorer (WISE; Wright et al. 2010) data, as well as optical photometry available; iii) mostly very low-mass (VLM, $M_\star < 0.3 M_\odot$) objects, but also a number of more massive ($M_\star < 1 M_\odot$) stars, in order to explore a wider range of accretion luminosity.

The two main bibliographic sources from which our sample was compiled are Allen et al. (2007) and Merín et al. (2008). The former reports several new VLM young stellar and sub-stellar objects with Spitzer colors, while the latter provides a well characterised sample in terms of spectral energy distribution (SED) and SED spectral index, based on the Spitzer c2d criteria (Evans et al. 2009). Additional Class-II YSOs in Lupus-III that extend the sample to a broader mass range, and eventually to higher accretion luminosity, were selected from Hughes et al. (1994), following as close as possible criteria i) and ii) above, although several of these targets do not possess Spitzer fluxes because they were not covered by the c2d or other Spitzer surveys. Thus, the available WISE data were used.

Among the selected objects, there are two visual binaries, namely Sz 88 and Sz 123, where both the components were observed by us. In other 8 of our YSOs the Spitzer images revealed objects with separation between $2''$ and $10''$ (see Table 1), among these 6 at separations larger than $4''$ (see Table 1 in Merín et al. 2008 and Table 9 in Comerón 2008). The spatial resolution of X-Shooter is sufficiently high, allowing the observation of all our targets without light pollution from any of those nearby objects. To our knowledge, none of our targets has been reported as a spectroscopic binary in previous investigations using high-resolution spectroscopy (e.g. Melo 2003; Guenther et al. 2007). Our sample also includes Par-Lup3-4, one of the lowest mass young stellar objects in Lupus known to host an outflow (Comerón et al. 2003). Although separate

X-Shooter papers are being devoted to studying outflows (Bacciotti et al. 2011; Whelan et al. 2013; Giannini et al. 2013), we include Par-Lup3-4 here to investigate its accretion properties in the same way as the other targets.

It must be stressed that, although the sample covers rather well the mass range between $\sim 0.05 M_\odot$ and $\sim 1 M_\odot$ (40% with $M_\star < 0.2 M_\odot$, 35% with M_\star in the range $0.2-0.5 M_\odot$, and 25% with $M_\star > 0.5 M_\odot$), it is incomplete at each mass bin. However, our sample represents about 50% of the total population of Class-II YSOs in the Lupus I and Lupus III clouds (see Table 6 by Merín et al. 2008, for the statistics of the different YSO Classes).

Table 1 provides the list of the targets. Ancillary photometric data, in the optical, near- and mid-IR, were collected from Allen et al. (2007), Merín et al. (2008), the WISE All-Sky Source Catalog and from an unpublished catalog by Comerón et al. (2009). Such data are reported in the on-line Tables C.1 and C.2 (published in electronic form only). Although not simultaneous with the X-Shooter spectroscopy, these are the only photometric data available that can be used for comparisons with the spectroscopic fluxes.

2.2. X-Shooter spectroscopy

With its three spectrograph arms, X-Shooter provides simultaneous wavelength coverage from ~ 300 to ~ 2480 nm. For most of the targets slits of $1.0/0.9/0.9$ arc-sec were used in the UVB/VIS/NIR arms, respectively, yielding resolving powers of 5100/8800/5600. Only the two brightest objects in the sample (Sz 74 and Sz 83) were observed through the $0.5/0.4/0.4$ arc-sec slits in the UVB/VIS/NIR arms, respectively, yielding resolving powers of 9100/17400/10500. Table 1 includes the log of observations. Most of the targets were observed in one cycle using the A-B nodding mode, while three (Lup 706, Par-Lup3-4, and 2MASS J16085953-3856275) were observed in two cycles using the A-B-B-A nodding mode. Several Class-III YSOs, indistinctly quoted here as Class-III YSOs or Class-III templates, were also observed throughout the various Italian-GTO star formation runs, and their properties were published in separate papers (Manara et al. 2013a; Stelzer et al. 2013b). The spectra of such stars are used as templates for the modelling of Balmer and Paschen continua (Section 4.1.1) and to estimate extinction and revisit the spectral types (Section 3) of the Class-II YSOs. The Class-III templates cover rather well the spectral range from K5 to M9 (see Manara et al. 2013a).

Except for a few minutes of thin cirrus when the seeing was ~ 1.3 arc-sec (only for Sz 130) and some clouds at the end of the night on April 06, 2010 (but only for the Class-III YSOs Par-Lup3-1 and Par-Lup3-2, see Manara et al. 2013a), the weather conditions were mostly photometric with sub-arcsecond seeing.

With a few exceptions explained next, all the targets were observed at parallactic angle. The components of Sz 88 and Sz 123, with separation $1''.49$ and $1''.70$, respectively, were observed simultaneously by aligning the 11 arc-sec slit at their position angle. Likewise, in the case of Par-Lup3-4 the slit was aligned at the position angle of the outflow (Bacciotti et al. 2011; Whelan et al. 2013).

Several telluric standard stars were observed with the same instrumental set-up and at very similar airmass as

Table 1. Selected YSOs and observing log.

Object/Other name	RA(2000) h :m :s	DEC(2000) ° ' "	Obs. Date YY-MM-DD	MJD (+2400000)	T_{exp} (sec)			S/N ratio ‡			Lupus cloud
					UVB	VIS	NIR	UVB	VIS	NIR	
Sz66†	15:39:28.28	-34:46:18.0	2012-04-18	56035.2516	2x300	2x250	2x100	40	140	55	I
AKC2006-19	15:44:57.90	-34:23:39.5	2011-04-23	55674.1966	2x900	2x900	2x900	7	50	40	I
Sz69 / HW Lup†	15:45:17.42	-34:18:28.5	2011-04-23	55674.0991	2x300	2x300	2x300	12	70	60	I
Sz71 / GW Lup	15:46:44.73	-34:30:35.5	2012-04-18	56035.0949	2x300	2x250	2x100	40	110	52	I
Sz72 / HM Lup	15:47:50.63	-35:28:35.4	2012-04-18	56035.1926	2x300	2x250	2x100	33	95	39	I
Sz73	15:47:56.94	-35:14:34.8	2012-04-18	56035.2923	2x300	2x250	2x100	20	115	55	I
Sz74 / HN Lup	15:48:05.23	-35:15:52.8	2012-04-18	56035.1695	2x150	2x100	2x50	22	135	45	I
Sz83 / RU Lup	15:56:42.31	-37:49:15.5	2012-04-18	56035.1794	2x100	2x50	2x30	45	130	50	I
Sz84	15:58:02.53	-37:36:02.7	2012-04-18	56035.1083	2x350	2x300	2x115	40	120	80	I
Sz130	16:00:31.05	-41:43:37.2	2010-04-07	55293.3609	2x300	2x300	2x300	40	90	45	IV
Sz88A (SW) / HO Lup (SW)	16:07:00.54	-39:02:19.3	2012-04-18	56035.3342	2x300	2x250	2x100	60	110	50	I
Sz88B (NE) / HO Lup (NE)	16:07:00.62	-39:02:18.1	2012-04-18	56035.3342	2x300	2x250	2x100	18	75	48	III
Sz91	16:07:11.61	-39:03:47.1	2012-04-18	56035.3213	2x300	2x250	2x300	40	70	35	III
Lup713†	16:07:37.72	-39:21:38.8	2010-04-06	55292.1950	2x900	2x900	2x900	8	50	45	III
Lup604s	16:08:00.20	-39:02:59.7	2010-04-06	55292.2374	2x450	2x450	2x450	5	60	40	III
Sz97	16:08:21.79	-39:04:21.5	2011-04-23	55674.1139	2x300	2x300	2x300	15	120	55	III
Sz99	16:08:24.04	-39:05:49.4	2010-04-07	55293.3452	2x300	2x300	2x300	14	60	35	III
Sz100†	16:08:25.76	-39:06:01.1	2011-04-23	55674.1391	2x300	2x300	2x300	10	50	55	III
Sz103	16:08:30.26	-39:06:11.1	2011-04-23	55674.1542	2x300	2x300	2x300	15	80	50	III
Sz104	16:08:30.81	-39:05:48.8	2010-04-06	55292.2549	2x300	2x300	2x300	10	70	50	III
Lup706	16:08:37.30	-39:23:10.8	2010-04-06	55292.2796	4x900	4x900	4x900	6	20	30	III
Sz106	16:08:39.76	-39:06:25.3	2012-04-18	56035.3051	2x450	2x400	2x450	36	85	50	III
Par-Lup3-3	16:08:49.40	-39:05:39.3	2010-04-06	55292.3586	2x300	2x300	2x300	5	50	30	III
Par-Lup3-4†	16:08:51.43	-39:05:30.4	2010-04-07	55293.1763	4x900	4x900	4x900	7	30	45	III
Sz110 / V1193 Sco	16:08:51.57	-39:03:17.7	2011-04-23	55674.3413	2x300	2x300	2x300	35	103	55	III
Sz111 / Hen 3-1145	16:08:54.69	-39:37:43.1	2012-04-18	56035.1229	2x300	2x250	2x100	50	90	45	III
Sz112	16:08:55.52	-39:02:33.9	2012-04-18	56035.2644	2x350	2x300	2x350	20	40	35	III
Sz113	16:08:57.80	-39:02:22.7	2011-04-23	55674.3566	2x900	2x900	2x900	15	70	38	III
2MASS J16085953-3856275†	16:08:59.53	-38:56:27.6	2011-04-23	55674.2808	4x900	4x900	4x900	5	18	20	III
SSTc2d160901.4-392512	16:09:01.40	-39:25:11.9	2011-04-23	55674.2260	2x450	2x450	2x450	20	80	45	III
Sz114 / V908 Sco	16:09:01.84	-39:05:12.5	2011-04-23	55674.3850	2x300	2x300	2x300	30	90	30	III
Sz115	16:09:06.21	-39:08:51.8	2012-04-18	56035.3469	2x350	2x300	2x350	20	70	45	III
Lup818s†	16:09:56.29	-38:59:51.7	2011-04-23	55674.2442	2x900	2x900	2x900	5	25	33	III
Sz123A (S)	16:10:51.34	-38:53:14.6	2012-04-18	56035.2784	2x700	2x600	2x350	25	60	45	III
Sz123B (N)	16:10:51.31	-38:53:12.8	2012-04-18	56035.2784	2x700	2x600	2x350	25	70	35	III
SST-Lup3-1†	16:11:59.81	-38:23:38.5	2010-04-06	55292.3781	2x450	2x450	2x450	6	35	40	III

Notes. † : nearby ($2'' < d < 10''$) object detected in the Spitzer images (see Merín et al. 2008; Comerón 2008).

‡ : the S/N ratio refers to the central wavelength of each spectrograph arm.

the targets. Normally two flux standards per night were observed through a 5 arcsec slit for flux calibration purposes.

2.3. Data reduction

The data reduction was done independently for each spectrograph arm using two versions of the X-Shooter pipeline (Modigliani et al. 2010), depending on the period in which the data were acquired: version 1.0.0 was used for the April 2010 data, while for the data acquired in April 2011 and April 2012 version 1.3.7 was used. The standard steps of processing included bias or dark subtraction, flat fielding, optimal extraction, wavelength calibration, and sky subtraction. Since version 1.0.0 did not include flux calibration, a MIDAS¹ routine (see details in Alcalá et al. 2011) was used for the April 2010 data. Wavelength shifts due to instrumental flexure were corrected using the *flexcomp*

package within the pipeline. The precision in wavelength calibration is better than 0.01 pix in the UVB and VIS arms, corresponding to 0.002 nm, but errors can be as large as ~ 0.006 nm in the NIR arm. The flux calibration for the April 2011 and April 2012 data was done using the pipeline. A test data-set was processed with both the MIDAS procedure and the pipeline, confirming that the flux-calibrated spectra resulting from both procedures are identical. The final extracted one-dimensional flux-calibrated spectra, from the MIDAS procedure or the pipeline, are not corrected for telluric absorption bands. The telluric correction was performed independently in the VIS and NIR spectra as explained in Appendix A. The X-Shooter scale of ~ 0.16 arc-sec/pix along the slit direction allowed to resolve the components of the binaries, making possible the extraction of the spectra of the individual components, without any light contamination.

By comparing the response function of different flux standards observed during the same night, we estimate an intrinsic precision on the flux calibration of $\sim 5\%$. This does not consider, however, errors due to flux losses induced by

¹ The Munich Image Data Analysis System (MIDAS) provides general tools for image processing and data reduction. It is developed and maintained by the ESO.

seeing variations during the science exposures. Such errors are expected to be small (less than 10%), as the seeing was always sub-arcsecond during the science exposures. In the case of Sz 74 and Sz 83, both observed with the narrow slits, the seeing was ~ 0.5 arc-sec. Therefore, $\sim 10\%$ can be considered as a robust relative error for the flux calibration.

The overlap of ~ 40 nm between the UVB-VIS and VIS-NIR spectra allows us to verify the consistency in flux between the different arms. While the flux match between the UVB and VIS spectra is always perfect, the NIR flux in some cases is low with respect to the VIS flux by a factor $< 1.2^2$. Thus, an additional correction was applied to the NIR spectrum to match the flux in the VIS arm.

Finally, the ancillary photometric data were used to compare the spectroscopic fluxes with the photometric ones. The spectra follow the corresponding SED shape very well, with most of them matching the photometric fluxes within a factor of less than 1.5, whereas in some cases of objects well known to be strongly variable (c.f. Par-Lup3-4, Sz 74, Sz 83, Sz 106, Sz 113) the ratio may be as large as 2.5. In these latter cases the difference between photometric and spectroscopic fluxes can be ascribed to variability of the object.

3. Stellar and sub-stellar properties

Estimates of the physical parameters exist in the literature for some of the YSOs in our sample, but they are unknown for the majority of our targets. The quality and performance of the X-Shooter spectra allow us to derive many physical quantities (c.f. Manara et al. 2013b). In this paper, however, we focus only on those parameters strictly needed to study the accretion properties of our sample. Examples of full exploitation of the X-Shooter spectra for brown dwarfs and YSOs can be found in Alcalá et al. (2011), Stelzer et al. (2012), Manara et al. (2013a) and Stelzer et al. (2013a,b).

3.1. Spectral type

For the M-type stars various spectral indices were calculated following Riddick et al. (2007) for optical wavelengths, and the H₂O-K₂ index from Rojas-Ayala et al. (2012) for the near-IR spectra. The Riddick et al. (2007) spectral indices in the VIS are almost extinction independent³. The spectral type assigned to a given object was estimated as the average spectral type resulting from the various indices in the VIS. From the dispersion over the average of all the available spectral indices we obtain an uncertainty of half a spectral subclass.

The NIR indices provide spectral types which are consistent with the VIS results typically within one spectral sub-class. Thus, the spectral types derived from the VIS are adopted for the analysis, consistently with the spectral type assignment for the Class-III templates (Manara et al. 2013a). The spectral types are listed in Table 2. For both the earliest-type stars in our sample (Sz73 and Sz83), an accurate spectral type of K7 is reported in the literature (see

² Some flux losses in the NIR may result due to slit vignetting caused by a slight misalignment of the NIR slit with respect to the VIS and UVB arms.

³ Note that the spectral indices may be affected by high extinction ($A_V > 5$ mag). Worth to say that none of our targets has such high A_V .

Herczeg & Hillenbrand 2008; Comerón 2008). We revisit, however, the determination using the procedures described in Section 3.2.

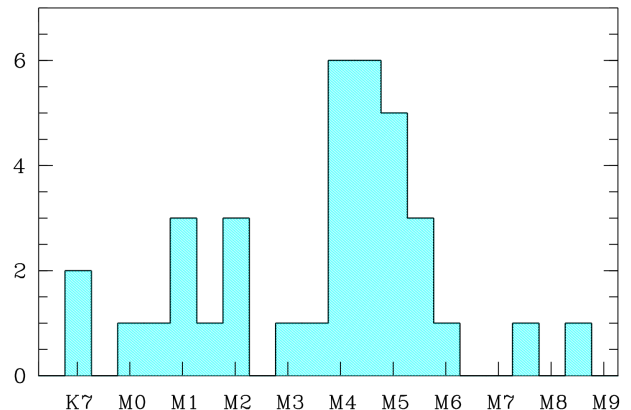


Fig. 1. Distribution of spectral types of the YSO sample.

Some difference in spectral type determinations in the literature can be ascribed to the different spectral ranges used in the different investigations (Comerón et al. 2003; Hughes et al. 1994; Mortier et al. 2011). With the wide spectral range of X-Shooter we can overcome this problem. In Appendix B we investigate the impact of veiling on the spectral indices, and conclude that for all M-type YSOs veiling is estimated to influence spectral type classification to less than 0.3 spectral subclasses, i.e. well within the uncertainty of spectral type determinations using spectral indices. Generally, our spectral types are consistent within ± 0.5 sub-class with those in the literature, with a few exceptions that are discussed at the end of the next section. The range of spectral types of our sample is from K7 to M8, with an over-abundance of M4-M5 objects (see Figure 1).

3.2. Extinction

To derive the extinction, A_V , for a given Class-II YSO, its VIS spectrum was compared with the Class-III templates best matching the Class-II spectral type. All our Class-III templates have low extinction ($A_V < 0.5$) (see Manara et al. 2013a). The templates were then artificially reddened by $A_V = 0 \dots 4.0$ mag, in steps of 0.25 mag, until the best match to the Class-II YSO was found. To redden the spectra we used the extinction law by Weingartner & Draine (2001), which covers a wide range in wavelength, from the UV to the mid-IR, and has also been adopted for the c2d investigations (see Evans et al. 2009). The procedure simultaneously provided a further test for the correct assignment of the template to derive the accretion luminosity (see Section 4.1.1). The A_V values derived in this way are listed in Table 2. We confirm that the majority of the targets possess zero extinction, as they were selected with this criterion. The highest values, 2.2 mag and 3.5 mag, are found for Par-Lup3-3 and Sz73, respectively.

The main sources of uncertainty on A_V are the errors in spectral type when associating a template to a given YSO and the error in the extinction of the template. The combined effect leads to an error of < 0.5 mag. However, an-

other important source of uncertainty may be introduced by strong veiling, which makes the YSOs spectra intrinsically bluer than the templates. In Appendix B we investigate this effect using the object with the strongest veiling among the M-type YSOs in our sample, i.e. Sz 113 (see Section 4.1.1) and conclude that in this case we may underestimate A_V by less than ~ 0.5 mag. Thus, the extinction as derived above is not severely affected by the veiling in our sample, but in order to minimize the impact of veiling the extinction was derived only from the red portion of the spectra starting at 600 nm. For earlier type stars ($< K7$) with much higher levels of veiling than those in our sample, other methods to derive extinction must be used (see for instance Manara et al. 2013b).

To check the self-consistency of the extinction derived in another spectral range we repeated the same procedure on the NIR spectra. The result is that the A_V values are consistent within the 0.5 mag uncertainty, but affected by a larger error (~ 0.75 mag). The latter is mainly due to the higher uncertainty in the spectral type provided by the spectral indices in the NIR than in the VIS. Thus, the values derived from the VIS are adopted for the following analysis. Another obvious reason for preferring the extinction in the VIS is that the extinction in the NIR is small and one needs to multiply it (and its uncertainty) by a large factor to derive A_V .

Our spectral type and extinction determinations are in good agreement with the literature values, except in a few cases. For Sz 69, Hughes et al. (1994) give a spectral type M1 with a visual extinction of 3.20 mag, while in our case the M4 template with zero extinction fits much better the entire X-Shooter spectrum. For Sz 110, Hughes et al. (1994) give M2, while Mortier et al. (2011) claim M3, more consistent with our M4 determination. In the case of Sz 113, the M4 spectral type reported by Hughes et al. (1994) agrees with our M4.5 determination, while Mortier et al. (2011) report M1 and Comerón et al. (2003) M6. The visual extinction values in the literature for Par-Lup3-4 range from 2.4 to 5.6 mag (Comerón et al. 2003). The confirmed under-luminosity and edge-on geometry of this object (Comerón et al. 2003; Huelamo et al. 2010) suggest that our zero extinction can be interpreted as wavelength-independent, i.e. gray extinction, rather than as a null extinction (Whelan et al. 2013). Interestingly, a null extinction is consistent with the value derived off-source using the [Fe II] lines at 1.27, 1.32, 1.64 μm (Bacciotti et al. 2011; Giannini et al. 2013), that trace jet emission (Nisini et al. 2005).

On the other hand, it is worth mentioning that the zero extinction we find for Sz 83 agrees with the value derived by Herczeg et al. (2005) from the profile of the Ly α line. Our procedure also confirms the spectral type of this YSO, despite its strong veiling (see Section 4.1.1). Also, our A_V determination for Sz 113, the most veiled among the M-type YSOs in our sample, agrees with the one by Hughes et al. (1994).

3.3. YSOs physical parameters

The effective temperature, T_{eff} , was derived using the temperature scales given by Kenyon & Hartmann (1995) for the two K-type stars, and by Luhman et al. (2003) for the M-type YSOs. The latter scale is intermediate between the dwarf and giant temperature scales, and more appropriate for young objects than temperature scales derived for

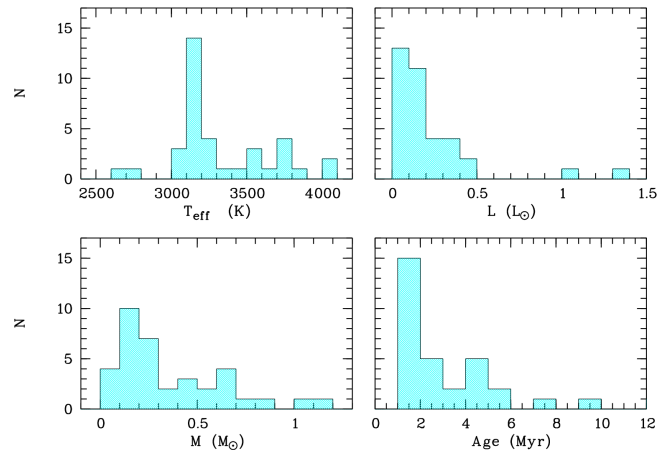


Fig. 2. Histograms of YSOs properties. The YSOs in the sample are cooler than 4000 K with 70% cooler than 3500 K. The vast majority have a luminosity of less than $0.5 L_{\odot}$, while more than 70% have a mass lower than $0.5 M_{\odot}$. Two YSOs (Lup 713 and Lup 818s) have a mass just at the hydrogen burning limit, while other two (Lup 706 and SST c2d160901.4-392512) are definitely sub-stellar.

field M dwarfs (e.g. Testi 2009; Rajpurohit et al. 2013). The stellar luminosity and radius were computed using the methods described in Spezzi et al. (2008), adopting the extinction and distance values given in Table 2. The stellar radius has also been determined using the flux-calibrated X-Shooter spectra as explained in Alcalá et al. (2011). The good agreement between the radius calculated with the two methods (c.f. Figure 5 in Alcalá et al. 2011) further confirms the reliability of the flux calibration of the spectra. Mass and age were derived by comparison with theoretical PMS evolutionary tracks (Baraffe et al. 1998; Chabrier et al. 2000) on the HR diagramme. The physical parameters of the targets are listed in Table 2 and summarised in Figure 2. Uncertainties in luminosity, radius and mass take into account the error propagation of about half spectral sub-class in spectral typing, as well as errors in the photometry and uncertainty on extinction.

The luminosity of four objects, namely Par-Lup3-4, Lup706, Sz 123B, and Sz 106, is significantly lower than for the other YSOs of similar spectral type or mass, hence their age results apparently older than 15 Myr. The sub-luminosity of these objects in comparison with the others is evident in Figure 3, where the HR-diagramme for the sample is shown. It is not entirely clear whether the relatively low-luminosity of these objects is due to evolution or to obscuration effects because of a particular disc geometry. Sub-luminosity has been reported for Sz 106 and Par-Lup3-4 (Comerón et al. 2003), and for the latter it has been shown that the disc is edge-on (Huelamo et al. 2010). No evidence of sub-luminosity for the other two objects is found in the literature. At the end of the paper (Section 7.4) we provide arguments suggesting that the sub-luminosity of these objects is most likely due to geometrical effects.

The average age of 3 ± 2 Myr for the sample, excluding the sub-luminous objects⁴, is consistent with previous age estimates for Lupus YSOs (Comerón 2008, and refer-

⁴ Note that these objects are not included in the age histogramme in Figure 2.

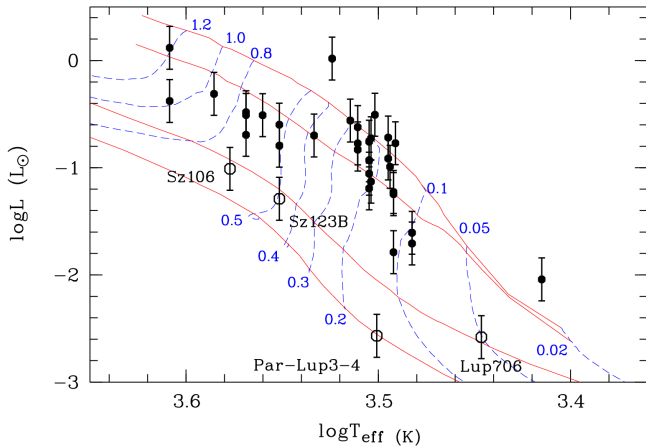


Fig. 3. Hertzsprung-Russell diagramme for the Lupus sample. The four sub-luminous objects described in the text are represented with open circles as labelled. The continuous lines show the 1 Myr, 3 Myr, 30 Myr and 10 Gyr isochrones by Baraffe et al. (1998), while the dashed lines show the low-mass Pre-Main Sequence evolutionary tracks by the same authors as labelled.

ences therein). We do not detect statistically significant differences among the stellar parameters of the Lupus-I and Lupus-III YSOs because our number statistics is small and this work deals only with Class-II YSOs. Note, however, that a recent investigation (Rygl et al. 2013) based on Herschel data of significant samples of all classes of YSOs, concludes that there are differences in the star formation rate between the various Lupus clouds.

Finally, the Li I $\lambda 670.78\text{nm}$ absorption line is detected in all the spectra, and it is identified for the first time in nine of our targets, two of which are part of the Class-III sample (Manara et al. 2013a). Among these nine, three objects previously considered only as candidates were confirmed to be truly YSOs. We also stress that for the stars Sz105 and Sz94, originally included in the X-Shooter observations, no lithium absorption was detected, despite the high S/N of their spectra. Therefore, they are not considered in our analysis. The nature of the Class-III source Sz94 has been discussed in Manara et al. (2013a) and Stelzer et al. (2013b), whereas the YSO nature of Sz105 is unclear, but will be discussed in a future work.

4. Accretion diagnostics

The energy loss per unit time of the accretion energy, or accretion luminosity L_{acc} , shows up as continuum and line emission over a wide spectral range. The contribution of the lines to L_{acc} is generally ignored because the continuum emission is normally larger, but as will be seen in Section 4.5, significant energy losses also occur in line emission. In this section we derive the accretion luminosity of each YSO in our sample from the continuum-excess measurements, that we describe as the continuum emission of a slab of hydrogen. Previous determinations of L_{acc} in the literature have also excluded line emission from estimates of the accretion excess emission, making our results directly comparable to those earlier studies. The slab modelling accounts also for the excess emission short-ward 330nm, which is about the shortest wavelength into which our spectra are

useful, and allows us to describe the excess emission in the Paschen continuum, where it is measured at very few wavelengths only, as line veiling.

4.1. Continuum emission

In accreting YSOs the continuum excess emission is most easily detected as Balmer continuum emission (see Valenti et al. 1993; Gullbring et al. 1998; Herczeg & Hillenbrand 2008; Rigliaco et al. 2012, and references therein). Except for two very low-mass objects (Lup604 and Par-Lup3-3), with rather noisy UVB spectra, Balmer continuum emission is evident in all the YSOs of our sample (see examples in Figure 4). The observed Balmer jump, BJ_{obs} , i.e. the ratio of the flux at 360 nm to the flux at 400 nm, ranges from 0.4 to 3.7 (c.f. Table 3), with only three objects (Lup604, Par-Lup3-3 and Sz112) having $\text{BJ}_{\text{obs}} \leq 0.5$. This satisfies the criterion suggested by Herczeg & Hillenbrand (2008) that any mid M-type dwarf with an observed Balmer jump greater than 0.5 should be considered an accretor. The intrinsic Balmer jump, BJ_{intr} , which is the ratio of the flux at 360 nm to the flux at 400 nm after extinction correction and subtraction of the photospheric emission, was calculated using the photospheric spectrum of the same Class-III template as in the slab modelling described below.

Paschen continuum emission (in the wavelength range from 364nm to 820nm) is dimmer than the Balmer emission in the UVB range, but is detected as veiling of the photospheric lines. Examples of such filling-in of the Ca I $\lambda 422.7\text{nm}$ absorption line in some of the YSOs in $\sigma\text{-Ori}$ are shown in Figure 3 by Rigliaco et al. (2012) (see also Figure 2 in Herczeg & Hillenbrand 2008). The filling-in of this line may be partially due to the Fe I emission lines at 421.6, 422.7 and 423.3 nm. The continuum emission at wavelengths longer than about 700 nm is rather weak in very low-mass YSOs and is hardly detected in many of our targets.

4.1.1. Calculation of continuum accretion luminosity

Following Valenti et al. (1993), Herczeg & Hillenbrand (2008) and Rigliaco et al. (2012), the spectrum of each Class-II YSO is fitted as the sum of the photospheric spectrum and the emission of a slab of hydrogen; the accretion luminosity is given by the luminosity emitted by the slab. We take the photospheric spectrum to be that of the Class-III template best matching the spectral type of the Class-II YSO reported in Table 2. The input spectra are extinction corrected using the extinction values reported in Table 2. The hydrogen slab emission includes bound-free and free-free emission from H and H^- ; it is computed assuming LTE conditions and is described by three parameters, namely the electron temperature and density and the slab length, which is related to the optical depth at 300 nm. These three parameters determine the wavelength dependence of the excess emission. In addition, there are two "normalization" parameters one for the slab emission and one for the Class-III template flux. We vary these 5 parameters over a wide range of values to find the model that best matches the observed continuum of the target spectrum. More specifically, we consider a number of spectral features, namely the observed Balmer jump, the slope of the Balmer continuum measured between ~ 340 and 360 nm, the slope of

Table 2. Spectral types, extinction, and physical parameters

Object	SpT	T_{eff} [K]	A_v [mag.]	d [pc]	L_* [L_{\odot}]	R_* [R_{\odot}]	M_* [M_{\odot}]	Age [Myr]	Notes
Sz66	M3.0	3415	1.00	150	0.200±0.092	1.29±0.30	0.45 ^{+0.05} _{-0.15}	4	
AKC2006-19	M5.0	3125	0.00	150	0.016±0.008	0.44±0.10	0.10 ^{+0.03} _{-0.02}	13	1, 2
Sz69	M4.5	3197	0.00	150	0.088±0.041	0.97±0.22	0.20 ^{+0.00} _{-0.03}	3	
Sz71	M1.5	3632	0.50	150	0.309±0.142	1.43±0.33	0.62 ^{+0.02} _{-0.17}	4	
Sz72	M2.0	3560	0.75	150	0.252±0.116	1.29±0.30	0.45 ^{+0.12} _{-0.00}	3	
Sz73	K7	4060	3.50	150	0.419±0.193	1.35±0.31	1.00 ^{+0.00} _{-0.00}	9	
Sz74	M3.5	3342	1.50	150	1.043±0.480	3.13±0.72	0.50 ^{+0.10} _{-0.10}	1	
Sz83	K7	4060	0.00	150	1.313±0.605	2.39±0.55	1.15 ^{+0.25} _{-0.05}	2	
Sz84	M5.0	3125	0.00	150	0.122±0.056	1.21±0.28	0.17 ^{+0.08} _{-0.02}	1	
Sz130	M2.0	3560	0.00	150	0.160±0.074	1.03±0.24	0.45 ^{+0.05} _{-0.00}	6	
Sz88A (SW)	M0	3850	0.25	200	0.488±0.225	1.61±0.37	0.85 ^{+0.10} _{-0.10}	4	
Sz88B (NE)	M4.5	3197	0.00	200	0.118±0.054	1.12±0.26	0.20 ^{+0.05} _{-0.03}	2	
Sz91	M1	3705	1.20	200	0.311±0.143	1.36±0.31	0.62 ^{+0.13} _{-0.08}	4	
Lup713	M5.5	3057	0.00	200	0.020±0.009	0.52±0.12	0.08 ^{+0.05} _{-0.00}	4	1
Lup604s	M5.5	3057	0.00	200	0.057±0.026	0.83±0.19	0.11 ^{+0.04} _{-0.02}	2	
Sz97	M4.0	3270	0.00	200	0.169±0.078	1.34±0.28	0.25 ^{+0.05} _{-0.00}	2	
Sz99	M4.0	3270	0.00	200	0.074±0.034	0.89±0.20	0.17 ^{+0.08} _{-0.00}	3	
Sz100	M5.5	3057	0.00	200	0.169±0.078	1.43±0.33	0.17 ^{+0.00} _{-0.04}	1	
Sz103	M4.0	3270	0.70	200	0.188±0.087	1.41±0.30	0.25 ^{+0.05} _{-0.00}	1	
Sz104	M5.0	3125	0.00	200	0.102±0.047	1.11±0.26	0.15 ^{+0.02} _{-0.02}	1	
Lup706	M7.5	2795	0.00	200	0.003±0.001	0.22±0.05	0.06 ^{+0.03} _{-0.02}	32	1, 3
Sz106	M0.5	3777	1.00	200	0.098±0.045	0.72±0.17	0.62 ^{+0.00} _{-0.05}	32	3
Par-Lup3-3	M4.0	3270	2.20	200	0.240±0.110	1.59±0.37	0.25 ^{+0.05} _{-0.05}	1	1
Par-Lup3-4	M4.5	3197	0.00	200	0.003±0.001	0.17±0.04	0.13 ^{+0.02} _{-0.00}	>50	1, 3
Sz110	M4.0	3270	0.00	200	0.276±0.127	1.61±0.37	0.35 ^{+0.05} _{-0.05}	1	
Sz111	M1	3705	0.00	200	0.330±0.152	1.40±0.32	0.75 ^{+0.05} _{-0.13}	6	
Sz112	M5.0	3125	0.00	200	0.191±0.088	1.52±0.35	0.25 ^{+0.00} _{-0.08}	1	
Sz113	M4.5	3197	1.00	200	0.064±0.030	0.83±0.19	0.17 ^{+0.03} _{-0.03}	3	
2MASS J16085953-3856275	M8.5	2600	0.00	200	0.009±0.004	0.47±0.11	0.03 ^{+0.04} _{-0.01}	1	1, 2
SSTc2d160901.4-392512	M4.0	3270	0.50	200	0.148±0.068	1.25±0.29	0.20 ^{+0.10} _{-0.05}	1	
Sz114	M4.8	3175	0.30	200	0.312±0.144	1.82±0.42	0.30 ^{+0.05} _{-0.10}	1	
Sz115	M4.5	3197	0.50	200	0.175±0.080	1.36±0.31	0.17 ^{+0.08} _{-0.08}	1	
Lup818s	M6.0	2990	0.00	200	0.025±0.011	0.58±0.13	0.08 ^{+0.02} _{-0.02}	3	1, 2
Sz123A (S)	M1	3705	1.25	200	0.203±0.093	1.10±0.25	0.60 ^{+0.20} _{-0.02}	7	
Sz123B (N)	M2.0	3560	0.00	200	0.051±0.024	0.58±0.13	0.50 ^{+0.03} _{-0.10}	40	3
SST-Lup3-1	M5.0	3125	0.00	200	0.059±0.027	0.85±0.19	0.13 ^{+0.02} _{-0.04}	2	

Notes.

1: Li I λ 670.78nm absorption line detected for the first time. The other two targets for which the line is seen for the first time are the Class-III YSOs Par-Lup3-1 and Par-Lup3-2 (see Manara et al. 2013a); **2:** YSO nature confirmed; **3:** sub-luminous YSO.

the Paschen continuum between ~ 400 and ~ 475 nm, the value of the observed fluxes at ~ 360 nm, ~ 460 nm, and ~ 710 nm. This includes spectral regions where the emission is likely to be dominated by the accretion shock emission and regions where the photospheric emission is likely the dominant component. The best-fit procedure is described in Manara et al. (2013b). After the best-fitting model has been found, we then check if it reproduces well other spectral features, in particular the Ca I λ 422.7 nm absorption line. Examples of slab modelling are shown in Figure 4 and the complete set of plots showing the fits for all targets are provided in electronic form only (Figures from C.1 to C.4).

The adopted Class-III templates, and the BJ_{obs} , BJ_{intr} , and L_{acc} values corresponding to each Class-II YSO are reported in Table 3. In this table we also give the ratio of the excess emission over the photospheric one at 710 nm as in the best-fit model. The uncertainties on L_{acc} are dominated by the uncertainty in the extinction and by the choice

of the Class-III template (Manara et al. 2013b). An additional, non-negligible uncertainty for low values of L_{acc} , comes from the uncertainty on the Paschen continuum excess emission, especially in objects with poor signal-to-noise (e.g. Rigliaco et al. 2012). In general, we estimate that the uncertainty on L_{acc} is ~ 0.2 dex.

The Balmer and Paschen continua, as well as the Balmer jump, are well reproduced by our fits. On the other hand, we stress that we did not attempt to fit the hydrogen emission lines but only the continuum emission. For this reason the region on the longer wavelength side of the Balmer jump ($\lambda \sim 365$ -370 nm) is not well reproduced by our fits, as the emission in this region originates from a superposition of unresolved hydrogen emission lines and not from continuum emission. In some cases, even when the lines are clearly resolved, the overlapping of their wings produce a pseudo-continuum that we do not account for. Such line blending shifts the apparent Balmer jump to ~ 370 nm, while the

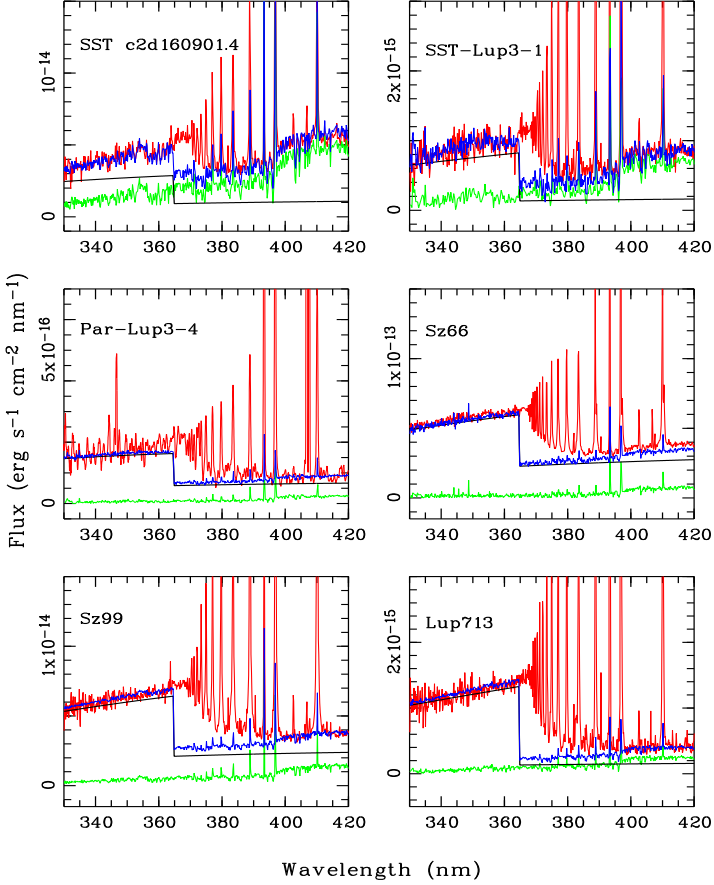


Fig. 4. Examples of X-Shooter spectra of Class-II YSOs in the region of the Balmer jump (red lines). The spectrum of the adopted Class-III templates are over-plotted with green lines. The continuum emission from the slab is shown by the black continuous line. The best fit with the emission predicted from the slab model added to the template is given by the blue lines.

actual jump is at 364.6 nm. In Section 4.5 we estimate the contribution of this effect on the total budget of the Balmer continuum emission.

Only in one case namely Sz123B, the slope of the Balmer continuum is not exactly reproduced by any combination of our free parameters. We checked that this is not due to data reduction problems (e.g. flat-field correction or incorrect spectrum extraction), but perhaps to slit-loss effects. Small differences between the observed and best-fit spectra in the Paschen continuum are present in some objects (e.g. AKC2006-19, Sz115), but differences are small compared to the excess emission in the Balmer continuum region. We were always able to fit our observations with a single slab model, without the necessity of multiple accretion components (Ingleby et al. 2013), and our fits reproduce well the observed spectra on a large wavelength interval, from ~ 330 nm to ~ 720 nm.

In about 50% of the objects, the excess emission in the Paschen continuum accounts for more than 50% of L_{acc} , and in all the targets at least 30% of the total excess is emitted in that region.

4.2. Mass accretion rate

The accretion luminosities were converted into mass accretion rates, \dot{M}_{acc} , using the relation:

$$\dot{M}_{\text{acc}} = \left(1 - \frac{R_{\star}}{R_{\text{in}}}\right)^{-1} \frac{L_{\text{acc}} R_{\star}}{GM_{\star}} \approx 1.25 \frac{L_{\text{acc}} R_{\star}}{GM_{\star}} \quad (1)$$

where R_{\star} and M_{\star} are the YSO radius and mass reported in Table 2, respectively, and R_{in} is the YSO inner-disc radius (Gullbring et al. 1998; Hartmann 1998). The latter corresponds to the distance from the star at which the disc is truncated – due to the stellar magnetosphere – and from which the disc gas is accreted, channelled by the magnetic field lines. It has been found that R_{in} ranges from $3R_{\star}$ to $10R_{\star}$ (Johns-Krull 2007). For consistency with previous studies (e.g. Gullbring et al. 1998; Herczeg & Hillenbrand 2008; Rigliaco et al. 2012), here we assume R_{in} to be $5R_{\star}$. The results on \dot{M}_{acc} , are listed in column 7 of Table 3.

We calculate \dot{M}_{acc} values from $2 \times 10^{-12} M_{\odot} \text{ yr}^{-1}$ to $4 \times 10^{-8} M_{\odot} \text{ yr}^{-1}$. The sources of error in \dot{M}_{acc} are the uncertainties on L_{acc} , stellar mass and radius (see Table 2). Propagating these, we estimate an average error of ~ 0.35 dex in \dot{M}_{acc} . However, additional errors on the aforementioned quantities come from the uncertainty in distance, as well as from differences in evolutionary tracks. The uncertainty on the Lupus YSOs distance is estimated to be $\sim 20\%$ (see Comerón 2008, and references therein), yielding a relative uncertainty of about 0.26 dex in the mass accretion rate⁵. On the other hand, using the D’Antona & Mazzitelli (1997) tracks we obtain a difference in mass from 10% to 70% (with an average of 30%) with respect to the Baraffe et al. (1998) tracks, leading to uncertainties of 0.04 dex to 0.3 dex in \dot{M}_{acc} . We estimate that the cumulative relative uncertainty in \dot{M}_{acc} is about 0.5 dex.

With $\dot{M}_{\text{acc}} = 3.4 \times 10^{-8} M_{\odot} \text{ yr}^{-1}$, the strongest accretor in our sample is Sz 83. A variety of \dot{M}_{acc} estimates for this star exist in the literature that range from 10^{-7} to a few $10^{-8} M_{\odot} \text{ yr}^{-1}$, and may be as high as 10^{-6} (Comerón 2008). Our \dot{M}_{acc} estimate is in very good agreement with that calculated by Herczeg & Hillenbrand (2008) ($1.8 \times 10^{-8} M_{\odot} \text{ yr}^{-1}$).

There are large discrepancies between our \dot{M}_{acc} determinations and those derived by Comerón et al. (2003) for Sz 100, Sz 106, Sz 113 and Par-Lup3-4. The Comerón et al. (2003) estimates, which are based on the flux of the Ca II $\lambda 854.2$ nm line, are larger by up to 1 dex. Although part of the discrepancies may be in principle ascribed to variable accretion, such variability must be enormous over timescales of years to explain the differences. Costigan et al. (2012) and Costigan et al. (2013) have observed variable accretion over years, but their results show that it is very rare to have YSOs that vary \dot{M}_{acc} by large factors. Most of the variability they find occurs on rotational timescales, suggesting asymmetric, rather than strongly variable accretion flows.

4.3. Emission lines

A large number of permitted and forbidden emission lines, displaying a variety of profiles, are detected. The analysis

⁵ Note that $\dot{M}_{\text{acc}} \propto d^3$, as $L_{\text{acc}} \propto d^2$ and $R_{\star} \propto d$.

Table 3. Accretion properties of Lupus YSOs.

Object	Template	BJ _{obs}	BJ _{intr}	logL _{acc} [L _⊙]	veiling at 710nm	logM _{acc} [M _⊙ yr ⁻¹]	L _{all_lines} /L _{acc}	WHα(10%) [km s ⁻¹]
Sz66	SO797	1.50	1.90	-1.8	0.45	-8.73	0.09	460
AKC2006-19	SO641	0.60	14.67	-4.1	0.04	-10.85	0.16	228
Sz69	SO797	2.83	4.50	-2.8	0.18	-9.50	0.55	403
Sz71	TWA15A	1.19	2.65	-2.2	0.08	-9.23	0.24	350
Sz72	TWA9B	2.73	3.70	-1.8	0.23	-8.73	0.28	455
Sz73	SO879	1.05	2.08	-1.0	0.22	-8.26	0.05	504
Sz74	TWA15A	0.90	1.46	-1.5	0.10	-8.09	0.07	401
Sz83	SO879	2.28	2.27	-0.3	1.88	-7.37	0.14	604
Sz84	SO641	1.44	2.65	-2.7	0.10	-9.24	0.28	456
Sz130	TWA2A	1.50	2.43	-2.2	0.15	-9.23	0.20	266
Sz88A (SW)	TWA25	2.08	3.03	-1.2	0.32	-8.31	0.18	597
Sz88B (NE)	SO797	0.87	3.34	-3.1	0.04	-9.74	0.18	405
Sz91	TWA13A	1.12	2.14	-1.8	0.12	-8.85	0.22	374
Lup713	Par-Lup3-2	3.50	6.50	-3.5	0.12	-10.08	0.54	378
Lup604s	SO925	0.50	8.50	-3.7	0.05	-10.21	0.13	264
Sz97	Sz94	1.00	3.70	-2.9	0.03	-9.56	0.38	452
Sz99	TWA9B	1.90	2.65	-2.6	0.26	-9.27	0.19	373
Sz100	SO641	0.87	2.16	-3.0	0.09	-9.47	0.31	251
Sz103	Sz94	0.74	1.87	-2.4	0.14	-9.04	0.09	426
Sz104	SO641	0.65	1.90	-3.2	0.06	-9.72	0.23	201
Lup706	TWA26	2.40	13.50	-4.8	0.11	-11.63	0.51	328
Sz106	TWA25	0.97	1.87	-2.5	0.14	-9.83	0.06	459
Par-Lup3-3	TWA15A	0.50	1.10	-2.9	0.01	-9.49	0.19	240
Par-Lup3-4	SO641	2.00	3.00	-4.1	0.25	-11.37	0.46	393
Sz110	Sz94	1.43	2.14	-2.0	0.26	-8.73	0.20	498
Sz111	TWA13A	1.36	9.60	-2.2	0.04	-9.32	0.41	455
Sz112	SO641	0.40	1.40	-3.2	0.03	-9.81	0.15	160
Sz113	SO797	1.86	2.29	-2.1	0.56	-8.80	0.20	392
2MASS J16085953-3856275	TWA26	3.69	15.00	-4.6	0.08	-10.80	0.39	147
SSTc2d160901.4-392512	Sz94	0.84	3.85	-3.0	0.04	-9.59	0.35	447
Sz114	Sz94	0.67	2.07	-2.5	0.05	-9.11	0.26	222
Sz115	SO797	0.53	1.00	-2.7	0.10	-9.19	0.07	338
Lup818s	SO925	1.06	4.00	-4.1	0.08	-10.63	0.48	200
Sz123A (S)	TWA2A	1.71	2.71	-1.8	0.22	-8.93	0.30	487
Sz123B (N)	TWA15B	1.36	2.45	-2.7	0.09	-10.03	0.36	519
SST-Lup3-1	SO641	1.23	6.00	-3.6	0.03	-10.17	0.48	254

of forbidden emission lines is deferred to a forthcoming paper (Natta et al. 2013, in prep). The emission lines studied here are listed in Table 4. The detection/non-detection of such lines depends on instrumental sensitivity and on the accretion rate of the individual YSO. The number of detections of each line is given in column 5 of Table 4, labelled as number of points used for the linear fits in Section 5.

The detected emission lines include several from the Balmer and Paschen series, the Br γ line, as well as several helium and calcium lines. Examples of permitted emission lines in X-Shooter spectra from our GTO programme have been published in previous papers (e.g. Alcalá et al. 2011; Bacciotti et al. 2011; Rigliaco et al. 2011c, 2012; Manara et al. 2013a; Stelzer et al. 2013a).

Balmer lines are detected up to H25 in six objects (Lup 713, Sz 113, Sz 69, Sz 72, Sz 83, Sz 88A). One among these (Lup 713) is at the hydrogen burning limit, with its spectrum resembling that of the young brown dwarf J053825.4-024241 reported in Rigliaco et al. (2011b). In Sz 88A Balmer line emission is detected up to H27 at the 2 σ level. The Pa 8, Pa 9 and Pa 10 are located in spectral regions of dense telluric absorption bands. Although the telluric correction has been performed as accurately as possible, some residuals from the correction still remain. Thus,

the detection and analysis of these three Paschen lines is more uncertain, leading to larger errors, in particular for Pa 8.

In this work we consider the nine He I lines with the highest transition strength. Among these, the He I λ 1082.9nm has been found to be also related to winds/outflows (Edwards et al. 2006). Thus, the line may include both the accretion and wind contributions. In most cases the He I λ 492.2nm is blended with the Fe I λ 492.1nm line and we did not attempt any de-blending.

The Ca II H & K lines are detected in all YSOs. The Ca II H-line is partially blended with He ϵ . The Ca II IRT $\lambda\lambda$ 849.8, 854.2, 866.2nm and the D-lines of the Na I $\lambda\lambda$ 589.0, 589.6nm doublet are very well resolved in all our spectra. In several objects both the Ca II IRT and the Na I lines show up as an emission reversal superposed on the broad photospheric absorption lines. Thus, the strength of these lines must be corrected for the photospheric contribution. This was done for the complete sample (see Section 4.4).

Finally, the two O I lines at 777.3nm and 844.6nm are well detected in 14 and 18 YSOs, respectively. These lines are seen in the objects with the strongest Balmer, He I and Ca II lines.

4.4. Line fluxes and equivalent widths

The flux in permitted lines was computed by direct integration of the flux calibrated and extinction corrected spectra, using the *splot* package under IRAF⁶. Three independent measurements per line were done, considering the lowest, highest, and middle position of the local continuum, depending on the local noise level of the spectra. The flux and its error were then computed as the average and standard deviation of the three independent measurements, respectively. The extinction-corrected fluxes, equivalent widths, and their errors are reported in several tables provided in electronic form only (from Table C.3 to C.11)⁷. In the cases where the lines were not seen, 3σ upper limits were estimated using the relationship $3 \times F_{\text{noise}} \times \Delta\lambda$, where F_{noise} is the rms flux-noise in the region of the line and $\Delta\lambda$ is the expected average line width, assumed to be 0.2 nm.

In the case of the H ϵ line, blended with the Ca II H line, measurements of both lines were attempted by a de-blending procedure using IRAF. In many cases, the X-Shooter resolution allows us to resolve both lines almost entirely. However, 11 YSOs display very broad lines, making the de-blending measurements unreliable. These objects are flagged in the electronic Tables C.3 and C.10.

The contribution of the photospheric absorption lines of the Na I D lines and the Ca II IRT, strongest in the late-K and early-to-mid M-type objects, have been removed in all the spectra by using the synthetic BT-Settl spectra by Allard et al. (2010) of the same T_{eff} and $\log g$ as the YSOs, binned at the same resolution of X-Shooter, and rotationally broadened at the same $v \sin i$ as the YSOs. For this purpose, the ROTFIT code (Frasca et al. 2006), specifically modified for X-Shooter data (See Stelzer et al. 2013b, for details), was applied. In some objects with very broad emission lines, the Ca II IRT lines are fully blended with the Paschen lines Pa 13 ($\lambda 866.502$ nm), Pa 15 ($\lambda 854.538$ nm) and Pa 16 ($\lambda 849.249$ nm). These objects are flagged in the electronic Table C.10.

We note that the ratio of the Ca II IR triplet lines is always very close to 1:1:1 (see the electronic Table C.10), i.e. consistent with optically thick gas conditions (Herbig & Soderblom 1980; Hamann & Persson 1992, and references therein), suggesting that the lines are formed in a high density region near the surface of the central YSO, rather than in a low-density outflow environment (see Reipurth et al. 1986; Graham & Heyer 1988; Fernández & Comerón 2001).

Although several objects display hydrogen recombination lines with high quantum numbers, here the analysis is restricted to Balmer lines up to H15, Paschen lines up to Pa 10 and the Br γ line, as well as the helium, calcium, sodium, and oxygen lines listed in Table 4.

The luminosity of the different emission lines was computed as $L_{\text{line}} = 4\pi d^2 \cdot f_{\text{line}}$, where d is the YSO distance in Table 2 and f_{line} is the extinction-corrected absolute flux of the lines reported in the electronic Tables C.3 to C.11.

⁶ IRAF is distributed by the National Optical Astronomy Observatory, which is operated by the Association of the Universities for Research in Astronomy, inc. (AURA) under cooperative agreement with the National Science Foundation

⁷ The flux errors reported in these tables are those resulting from the uncertainty in continuum placement. The estimated $\sim 10\%$ uncertainty of flux calibration (see Section 2.3) should be added in quadrature.

4.5. Lines versus continuum losses

We have calculated the total line luminosity, $L_{\text{all_lines}}$, as the sum of the luminosity of all the emission lines detected in every YSO. In the integrated luminosity of the Balmer lines we also account for the flux of the pseudo-continuum produced by line blending close to the Balmer Jump. The latter was measured by subtracting the flux of the best-fit model to the extinction-corrected spectrum of the YSO. On the average, more than 70% of the total line luminosity comes from the Balmer lines. In most cases (90%), the integrated Balmer line luminosity amounts to more than 60% of $L_{\text{all_lines}}$, while for a few objects with very strong lines (e.g. Sz 72, Sz 83, Sz 88 A, Sz 113) the emission in other lines may be as high as 55% of $L_{\text{all_lines}}$.

The integrated line luminosity is strongly correlated with L_{acc} (Figure 5). A linear fit yields: $\log(L_{\text{all_lines}}/L_{\odot}) = 0.86 \cdot \log(L_{\text{acc}}/L_{\odot}) - 1.05$, with a standard deviation $\sigma = 0.25$. This can be expressed as $\log(L_{\text{all_lines}}/L_{\text{acc}}) = -0.14 \cdot \log(L_{\text{acc}}/L_{\odot}) - 1.05$. From the latter equation and considering the scatter of the relation we calculate that objects with $L_{\text{acc}} < 10^{-4} L_{\odot}$ (only five YSOs) may have $L_{\text{all_lines}}/L_{\text{acc}}$ ratios as high as 0.55, while the ratio is lower for high L_{acc} and is < 0.25 for $L_{\text{acc}} > 10^{-3} L_{\odot}$. Column 8 of Table 3 lists the $L_{\text{all_lines}}/L_{\text{acc}}$ ratios. Although these numbers show that $L_{\text{all_lines}}$ is a fraction of L_{acc} , there is considerable emission also in the lines.

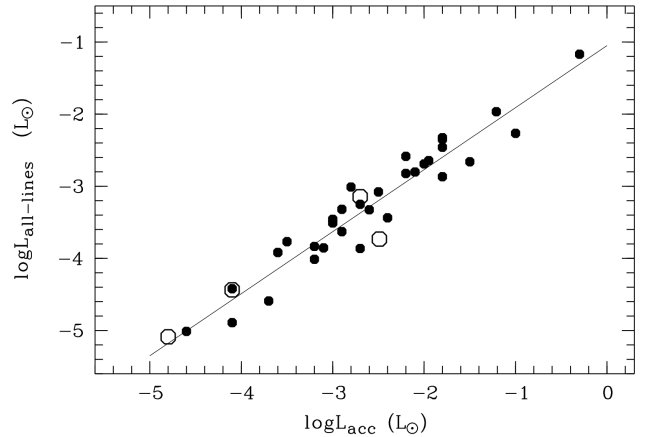


Fig. 5. Total emission line luminosity as a function of L_{acc} . The L_{acc} values were derived from the slab model in Section 4.1.1. Symbols are as in Figure 3. The continuous line represents the linear fit discussed in the text.

5. Relationships between continuum excess luminosity and emission line luminosity

In units of L_{\odot} , the dynamical range of L_{acc} for our sample covers more than four orders of magnitude, while the luminosity of the line diagnostics discussed in the previous section spans over more than five orders of magnitude. This allows us to investigate the relationships between continuum excess emission and the emission in individual permitted lines.

Table 4. Results of the $L_{\text{acc}} - L_{\text{line}}$ linear fits[†].

Diagnostic	λ [nm]	a (\pm err)	b (\pm err)	$N_{\text{points}}^{\ddagger}$	σ^*	No. upper limits	Comments
H3 (H α)	656.2800	1.12 (0.07)	1.50 (0.26)	36 + 6	0.36	0	
H4 (H β)	486.1325	1.11 (0.05)	2.31 (0.23)	36 + 6	0.27	0	•
H5 (H γ)	434.0464	1.09 (0.05)	2.50 (0.25)	36 + 6	0.27	0	•
H6 (H δ)	410.1734	1.06 (0.06)	2.50 (0.28)	36	0.30	0	•
H7 (H ϵ)	397.0072	1.07 (0.06)	2.64 (0.29)	36	0.30	0	1
H8	388.9049	1.04 (0.06)	2.55 (0.29)	36	0.30	0	•
H9	383.5384	1.01 (0.05)	2.53 (0.27)	36	0.29	0	•
H10	379.7898	1.00 (0.05)	2.58 (0.27)	35	0.29	1	•
H11	377.0630	1.02 (0.05)	2.74 (0.25)	35 + 6	0.27	1	•
H12	375.0151	0.99 (0.05)	2.73 (0.25)	35	0.26	1	•
H13	373.4368	1.00 (0.05)	2.85 (0.25)	34	0.25	2	•
H14	372.1938	1.02 (0.06)	3.09 (0.31)	31	0.25	5	•
H15	371.1977	1.02 (0.06)	3.13 (0.31)	31	0.25	5	•
Pa5 (Pa β)	1281.8070	1.04 (0.08)	2.45 (0.39)	29 + 6	0.38	7	•
Pa6 (Pa γ)	1093.8086	1.18 (0.06)	3.17 (0.31)	33 + 6	0.29	3	•
Pa7 (Pa δ)	1004.9368	1.18 (0.10)	3.33 (0.47)	25	0.36	9	•
Pa8	954.5969	1.11 (0.12)	3.19 (0.58)	17	0.39	16	
Pa9	922.9014	1.13 (0.09)	3.40 (0.47)	27	0.35	7	
Pa10	901.4909	1.03 (0.09)	2.99 (0.49)	26	0.39	8	
Br7 (Br γ)	2166.1210	1.16 (0.07)	3.60 (0.38)	19	0.28	14	•
He I	402.6191	1.04 (0.06)	3.62 (0.37)	31	0.27	5	•
He I	447.1480	1.05 (0.06)	3.45 (0.35)	33	0.30	3	•
He I	471.3146	1.04 (0.11)	4.25 (0.69)	16	0.29	12	•
He I Fe I	492.1931	0.90 (0.06)	2.65 (0.36)	32	0.31	4	2
He I	501.5678	0.98 (0.06)	3.36 (0.38)	30	0.27	4	•
He I	587.5621	1.13 (0.06)	3.51 (0.30)	36 + 6	0.28	0	•
He I	667.8151	1.16 (0.08)	4.12 (0.45)	36	0.36	0	•
He I	706.5190	1.14 (0.07)	4.16 (0.39)	36	0.32	0	•
He I	1082.9091	1.11 (0.12)	2.62 (0.57)	30	0.44	4	3
He II	468.5804	1.10 (0.09)	4.21 (0.57)	28	0.36	2	
Ca II (K)	393.3660	0.96 (0.05)	2.06 (0.27)	36	0.31	0	•
Ca II (H)	396.8470	1.02 (0.05)	2.37 (0.23)	36	0.25	0	4
Ca II	849.8020	0.95 (0.07)	2.18 (0.38)	34	0.41	2	
Ca II	854.2090	0.95 (0.08)	2.13 (0.42)	32	0.44	2	
Ca II	866.2140	0.95 (0.09)	2.20 (0.43)	29	0.43	4	
Na I	588.995	0.93 (0.06)	2.56 (0.32)	36	0.33	0	
Na I	589.592	0.90 (0.06)	2.56 (0.37)	36	0.38	0	
O I	777.3055	1.16 (0.09)	3.91 (0.51)	14	0.36	6	5
O I	844.6360	1.06 (0.18)	3.06 (0.90)	18	0.61	3	

Notes.

[†]: the relations are of the form $\log(L_{\text{acc}}/L_{\odot}) = a \cdot \log(L_{\text{line}}/L_{\odot}) + b$.

[‡]: number of points for the fit. The fits in which the six YSOs in σ -Ori (Rigliaco et al. 2012) were included are indicated with "+6". Although measurements of the Ca II IRT are also available in Rigliaco et al. (2012), we did not include them because those measurements were not corrected for the photospheric contribution. The number of points for Lupus is the number of YSOs in which the corresponding line was detected.

* : standard deviation from linear fit

Comments in last column: **(1)** partially blended with Ca II H; **(2)** He I + Fe I blend; **(3)** this line is also produced in winds/outflows (Edwards et al. 2006); the relationship must be used with caution.; **(4)** partially blended with He I; **(5)** O I $\lambda\lambda$ 777.194, 777.417nm doublet. •: Suggested relations for deriving L_{acc} from the line luminosity.

5.1. Continuum vs. line emission relationships

Electronic Figures C.5 to C.10 (on-line material only) show the relationships between L_{acc} and the luminosity of all the permitted emission lines discussed in Section 4.3. When

available, values of L_{acc} and L_{line} from previous investigations of YSOs in Taurus (c.f. Herczeg & Hillenbrand 2008, and references therein) and the σ -Ori cluster (Rigliaco et al. 2012) are overlaid.

Linear fits of the $\log L_{\text{acc}}$ vs. $\log L_{\text{line}}$ relationships have been calculated using the package ASURV (Feigelson & Nelson 1985) under the IRAF environment. ASURV includes censoring of upper or lower limits in the fits. In our various relationships the upper limits in the independent variable L_{line} are well consistent with the trends seen in the L_{acc} vs. L_{line} plots. The results of the fits (c.f. Table 4) with and without the inclusion of upper limits are consistent within the errors. The total number of points and the standard deviation of the fits are given in the fifth and sixth columns of Table 4, respectively. The errors in the computed relationships also account for upper limits when included. No fits were calculated for the Br 8 (Br δ) relation, as the number of upper limits is larger than the number of detections, and the relationship is very scattered (see electronic Figure C.7).

The trends in our L_{acc} vs. L_{line} relationships generally agree with those found in previous investigations (Muzerolle et al. 1998; Calvet et al. 2004; Natta et al. 2004; Herczeg & Hillenbrand 2008; Ingleby et al. 2013) (see electronic Figures C.5 to C.10). However, because of the different methodologies adopted to derive L_{acc} (H α line profile modelling, veiling in the FUV, UV and VIS, etc.), systematic differences may exist at different mass regimes (see Herczeg & Hillenbrand 2008, and next Section). Therefore, except for the YSOs in σ -Ori (Rigliaco et al. 2012), whose L_{acc} and L_{line} values were computed in the same way as here, we do not combine other literature data to derive L_{acc} - L_{line} relationships. Note also that our sample comprises $L_{\text{acc}} \leq 1 L_{\odot}$, while literature data extend to higher accretion luminosities.

While the accretion luminosity is well correlated with the luminosity of all the emission lines, the scatter in the correlations differs for the various lines (see standard deviation from the fits in Table 4).

5.2. Comparison with previous relationships

The electronic figures C.5 to C.10 show that the L_{acc} - L_{line} relations for the Lupus YSOs are fairly consistent with those in previous investigations of continuum-excess in YSOs in Taurus (c.f. Herczeg & Hillenbrand 2008, and references therein), and σ -Ori (Rigliaco et al. 2012). The slopes and zero points of the L_{acc} vs. L_{line} relations derived here are consistent within the errors with those reported in Herczeg & Hillenbrand (2008) (see their Table 16⁸). A comparison of the L_{acc} values derived here from the slab model with the average accretion luminosity drawn from different line diagnostics (e.g. H α , H β , H γ , H δ , the He I lines at 501.6nm and 587.6nm, the He II line at 468.5nm and the Ca II K line) as measured from the X-Shooter spectra (fluxes in electronic Tables C.3-C.11) and using the Herczeg & Hillenbrand (2008) relationships, leads to a rms difference <0.3 dex. This is significantly less than the error drawn from the application of single-diagnostic relationships (see also Rigliaco et al. 2012). We also note that our relationships for the H α , H β , and Ca II K lines are practically identical to those of Ingleby et al. (2013), which were derived by fitting UV and optical spectra with multiple accretion components.

⁸ Note that the slope and zero points in the Herczeg & Hillenbrand (2008) relationships are swapped in their Table 16.

Our L_{acc} - $L_{\text{Pa}\beta}$ and L_{acc} - $L_{\text{Br}\gamma}$ relations are also similar to those in previous works by Muzerolle et al. (1998), Natta et al. (2004), Calvet et al. (2000) and Calvet et al. (2004), but extend to much lower values of L_{acc} , toward the very low-mass regime (see electronic Figure C.7). As mentioned earlier, however, systematic differences may arise due to the different methodologies to derive L_{acc} . For instance, the difference in $\log L_{\text{acc}}$ when using our Br γ relationship and Muzerolle et al. (1998)'s may be up to ~ 0.5 dex for a typical $0.5 M_{\odot}$ T Tauri star with $L_{\text{Br}\gamma} \sim 10^{-3} L_{\odot}$.

5.3. Impact of chromospheric emission on L_{acc} estimates

Previous studies (Ingleby et al 2011; Rigliaco et al. 2012; Manara et al. 2013a) have stressed the impact of chromospheric emission on L_{acc} at low levels of accretion. Our estimates of L_{acc} are not influenced by chromospheric line emission, as they are derived from the continuum excess emission. The typical continuum emission of chromospheric origin, if present, is automatically corrected for by using as templates the Class-III stars, rather than field dwarfs.

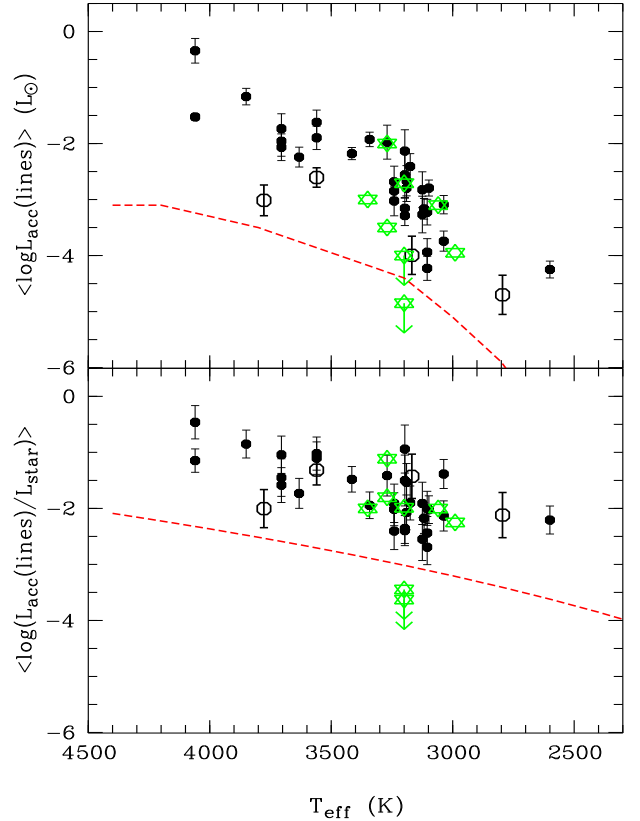


Fig. 6. The average accretion luminosity $\langle \log L_{\text{acc}}(\text{lines}) \rangle$ derived from 15 emission lines as described in the text (upper panel) and the $\langle \log L_{\text{acc}}(\text{lines})/L_{\star} \rangle$ ratio (lower panel) as a function of effective temperature for Lupus and σ -Ori (open stars) YSOs. Plotting symbols for the Lupus YSOs are as in Figure 3. The dashed lines in both panels mark the locus below which chromospheric emission is important in comparison with L_{acc} . The vertical error bars represent the standard deviation over the average of 15 emission line diagnostics.

In order to investigate the possible effects of chromospheric line emission in our sample, we derived the accretion luminosity, $L_{\text{acc}}(\text{lines})$, using emission line diagnostics and the $L_{\text{acc}}-L_{\text{line}}$ relations in Table 4. We calculate $\langle \log L_{\text{acc}}(\text{lines}) \rangle$ as the average over fifteen diagnostics discussed in Manara et al. (2013a). In Figure 6 the $\langle \log L_{\text{acc}}(\text{lines}) \rangle$ values and the $\langle \log L_{\text{acc}}(\text{lines})/L_{\star} \rangle$ ratio are plotted as a function of T_{eff} . The dashed lines in the figure show the level of chromospheric noise as determined by Manara et al. (2013a). Those lines represent the locus below which the contribution of chromospheric emission starts to be important in comparison with energy losses due to accretion. The accretion level of all the Lupus YSOs studied here is well above the chromospheric noise. Therefore, we conclude that the chromospheric contribution to L_{acc} is influential, even at the lowest values of L_{acc} . Our $L_{\text{acc}}-L_{\text{line}}$ relationships are hence calculated for L_{acc} values well above the chromospheric threshold. The two objects of σ -Ori indicated with upper limits correspond to SO 587 and SO 1266. For these two objects the fraction of luminosity in the Balmer lines with respect to the upper limit in L_{acc} is higher than one. Rigliaco et al. (2011a, 2012) show that in SO 587 the strong permitted lines probably originate in a photo-evaporation wind, while in SO 1266 they are dominated by chromospheric emission. We do not consider these two objects in the following plots and analysis.

6. Accretion properties

6.1. Accretion luminosity versus YSO luminosity

Previous investigations (e.g. Natta et al. 2006; Rigliaco et al. 2011a, and references therein) have shown that L_{acc} and stellar luminosity in Class-II YSOs are correlated, although with significant scatter at a given YSO luminosity. Clarke & Pringle (2006) pointed out that the distribution of points in the $L_{\text{acc}}-L_{\star}$ plane more or less fills a region which is bounded by the $L_{\text{acc}}=L_{\star}$ relation at high L_{acc} , but which is dominated by detection biases at low values of L_{acc} , roughly following a power-law $L_{\text{acc}} \propto L_{\star}^{1.6}$. This agrees with the relationships they derive from the data (detections and upper limits) in Natta et al. (2006). Tilling et al. (2008) presented simplified stellar evolution calculations for stars subject to time-dependent accretion history, and derived evolutionary tracks on the $L_{\text{acc}}-L_{\star}$ diagramme for a variety of fractional disc masses, $f_{\text{disc}} \equiv M_{\text{disc}}/M_{\star}$, and YSO masses. Using the D’Antona & Mazzitelli (1997) models, they assumed that the mass accretion rate declines with time as $t^{-\eta}$, with $\eta = 1.5$.

As shown in Figure 7, the Lupus YSOs also fall below the $L_{\text{acc}}=L_{\star}$ boundary, with a small number of objects between $0.1 L_{\odot}$ and $1 L_{\odot}$, and many with $L_{\text{acc}}/L_{\star} < 0.01$. The data points are apparently less scattered than those of previous samples. Our sample lacks YSOs with $L_{\text{acc}} > 1 L_{\odot}$, this being most likely the reason why we do not populate the region between $L_{\text{acc}}=0.1 L_{\star}$ and $L_{\text{acc}}=L_{\star}$ on the diagramme. The slope for the data in Figure 7 is steeper than the $L_{\text{acc}}/L_{\star} = \text{constant}$ lines, more or less following the slope of the Tilling et al. (2008) tracks. A linear fit to the data yields $L_{\text{acc}} \propto L_{\star}^{1.7}$, i.e. very similar to the claim by Clarke & Pringle (2006) for the lower envelope of the $L_{\text{acc}}-L_{\star}$ relation, but based on detections only. Note that Manara et al. (2012) find an almost identical power-law ($L_{\text{acc}} \propto L_{\star}^{1.68}$),

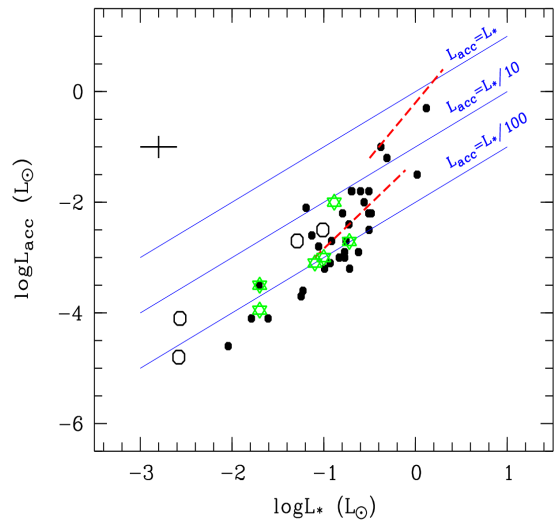


Fig. 7. Accretion luminosity as a function of stellar luminosity for Lupus and σ -Ori YSOs. Symbols are as in Figure 6. The two Lupus YSOs with the lowest luminosities are Par-Lup3-4 and Lup 706. The continuous lines represent the three L_{acc} vs. L_{\star} relations as labelled. Average error bars are shown in the upper left. The red dashed lines are the model tracks by Tilling et al. (2008) as follows: the upper line is for $1.0 M_{\odot}$ YSOs and $f_{\text{disc}} = 0.2$, while the lower one is for $0.4 M_{\odot}$ YSOs with $f_{\text{disc}} = 0.014$.

using a complete sample in the Orion Nebula Cluster, but with L_{acc} determinations based on deep photometry.

According to the Tilling et al. (2008) model and by a qualitative comparison between their evolutionary tracks and our data set on the $L_{\text{acc}}-L_{\star}$ diagramme (Figure 7), one would expect the discs of the lowest mass YSOs to have masses lower than $0.014 M_{\star}$. However, within the uncertainties of the measurements by Ricci et al. (2010), there is no evidence of a scaling between the disc mass and the stellar mass, or the mass accretion rate. Note also that a recent compilation for a wide range of masses suggests that the fractional disc mass is compatible with an uniform distribution around the value $f_{\text{disc}} \approx 0.01$ (Olofsson et al. 2013).

6.2. Accretion rate versus mass

Previous investigations (Muzerolle et al. 2003; Mohanty et al. 2005; Natta et al. 2006; Herczeg & Hillenbrand 2008; Rigliaco et al. 2011a; Antonucci et al. 2011; Biazzo et al. 2012, and references therein), have found that \dot{M}_{acc} goes roughly as the square of M_{\star} although with a significant scatter (up to 3 dex) in \dot{M}_{acc} for a given YSO mass.

Figure 8 shows the \dot{M}_{acc} versus M_{\star} diagramme for the Lupus YSOs studied here. The position of the σ -Ori stars in this plot is consistent with Lupus and the young brown dwarf FU Tau A, also investigated with X-Shooter (Stelzer et al. 2013a), follows the trend as well. The scatter is significantly increased by the four sub-luminous YSOs. A linear fit to the complete Lupus sample yields:

$$\log \dot{M}_{\text{acc}} = 1.89(\pm 0.26) \cdot \log M_{\star} - 8.35(\pm 0.18) \quad (2)$$

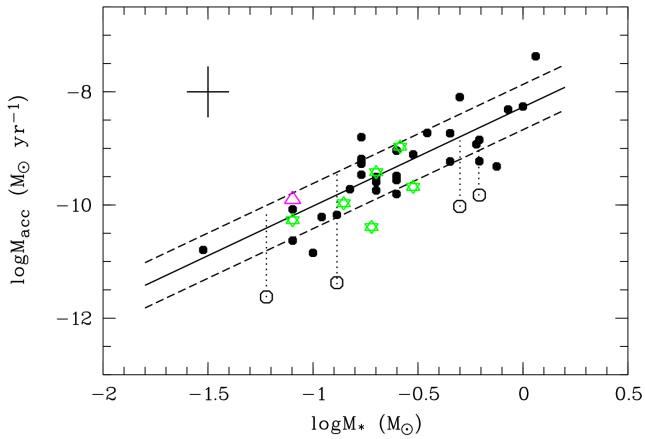


Fig. 8. Mass accretion rate \dot{M}_{acc} as a function of mass. Symbols are as in Figure 6. The vertical shifts in \dot{M}_{acc} for the low-luminosity YSOs (open circles), after correction for obscuration as explained in Section 7.4, are shown by the dotted lines. The big triangle represents the young brown dwarf FU Tau A, for which the \dot{M}_{acc} and M_{\star} values were derived by Stelzer et al. (2013a). The continuous line represents the linear fit of Equation 3, i.e. without including the sub-luminous objects. The dashed lines represent the 1σ deviation from the fit. Average error bars are shown in the upper left corner.

with a standard deviation of 0.6. The scatter decreases if the sub-luminous objects are excluded from the fit, yielding

$$\log \dot{M}_{\text{acc}} = 1.81(\pm 0.20) \cdot \log M_{\star} - 8.25(\pm 0.14) \quad (3)$$

with a standard deviation of 0.4. The slope and zero point of the $\dot{M}_{\text{acc}}-M_{\star}$ fit do not change significantly in either cases because the sub-luminous objects represent only 11% of our sample. It is thus reasonable to conclude that for our sample $\dot{M}_{\text{acc}} \propto M_{\star}^{1.8(\pm 0.2)}$, which is in agreement with previous studies (Natta et al. 2006; Muzerolle et al. 2005; Herczeg & Hillenbrand 2008; Rigliaco et al. 2011a; Antonucci et al. 2011; Biazzo et al. 2012; Manara et al. 2012), but inconsistent with the results by Fang et al. (2009) ($\dot{M}_{\text{acc}} \propto M_{\star}^3$) for their sub-solar mass sample in the Lynds 1630N and 1641 clouds in Orion. This inconsistency is more likely to be related to the different methodologies used to derive both \dot{M}_{acc} and M_{\star} rather than to different environmental conditions.

7. Discussion

7.1. Emission lines as tracers of accretion

Fitting the UV excess emission, and in general continuum excess emission, is the most reliable and accurate method to derive accretion luminosity in low-extinction YSOs (Muzerolle et al. 2003; Herczeg & Hillenbrand 2008; Rigliaco et al. 2012; Ingleby et al. 2013). In the absence of UV spectra, L_{acc} , hence \dot{M}_{acc} , can be calculated using emission line diagnostics. While the relationships by Herczeg & Hillenbrand (2008) are based on simultaneous low-resolution UV and optical spectroscopy, ours encompass and extend simultaneous observations of the diagnos-

tics from ~ 330 nm up to ~ 2500 nm, at intermediate spectral resolution.

Being based on almost twice the number of points as in previous works, the $L_{\text{acc}}-L_{\text{line}}$ relations computed here have in general a lower dispersion than those found in the literature applying similar methodologies (e.g. Herczeg & Hillenbrand 2008; Rigliaco et al. 2012; Ingleby et al. 2013). As in those works, each point in the relationships represents an instantaneous snapshot of L_{acc} and L_{line} . However, results of temporal monitoring of several YSOs indicate variability in optically thick line fluxes, without significant changes in the corresponding continuum accretion rate (e.g. Gahm et al. 2008; Herczeg et al. 2009), so that some dispersion may still arise from variability even when the observations are simultaneous. Long-term spectrophotometric monitoring of YSOs over a range of masses is still required to shed light on the magnitude of this effect.

The strongest line in optical spectra of YSOs is the $H\alpha$ line. Nevertheless, similarly as for the Taurus sample (Herczeg & Hillenbrand 2008), the $L_{\text{acc}}-L_{H\alpha}$ relation for the Lupus YSOs is the most scattered among the Balmer lines relationships (see Table 4). Not surprisingly, as it is well known that several other processes (e.g. outflows, hot spots, chromospheric activity, complex magnetic field topology and geometry, stellar rotation) besides accretion may contribute to the strength of the line. All these processes have an important impact on the line profile, in particular on its width. Previous investigations have used the full width of the $H\alpha$ line at 10% of the line peak, $WH\alpha(10\%)$ expressed in km s^{-1} , to investigate accretion (see White & Basri 2003; Natta et al. 2004, and references therein). Since $WH\alpha(10\%)$ is easily gathered from optical spectra, many authors have used it to estimate \dot{M}_{acc} . Nevertheless, as discussed by many authors, the relationship has a very large scatter and its use is discouraged when reliable measurements of the line luminosity are possible. In Natta et al. (2004) the \dot{M}_{acc} values used for low-mass stars ($< 0.3 M_{\odot}$) are based on modelling of the $H\alpha$ line profile (e.g. Muzerolle et al. 2001, 2003), whereas those for higher mass stars are mainly based on spectral veiling measurements (e.g. Gullbring et al. 1998).

In Figure 9 the $\dot{M}_{\text{acc}}-WH\alpha(10\%)$ scatter plot for the Lupus sample is compared with the Natta et al. (2004) relationship, represented with a continuous line. For objects with $WH\alpha(10\%) < 400 \text{ km s}^{-1}$, the Natta et al. (2004) relation tends to underestimate \dot{M}_{acc} with respect to our determinations from continuum-excess modelling by ~ 0.6 dex in $\log \dot{M}_{\text{acc}}$, on the average, but the differences may be up to about an order of magnitude. Similar differences were seen in the Herczeg & Hillenbrand (2008)'s Taurus sample and in the Fang et al. (2013, see their Figure 45) sample in the L1641 cloud. For objects with $WH\alpha(10\%) > 400 \text{ km s}^{-1}$, the slope of the Lupus correlation seems rather consistent with the Natta et al. (2004) relationship, but the $\log \dot{M}_{\text{acc}}$ values are systematically lower by $\sim 0.5-0.7$ dex. According to the Natta et al. (2004) relationship, YSOs with $WH\alpha(10\%) < 400 \text{ km s}^{-1}$ should have $\dot{M}_{\text{acc}} < 10^{-9} M_{\odot} \text{ yr}^{-1}$, and from Figure 8, these correspond to objects with $M_{\star} < 0.3 M_{\odot}$, i.e. those for which the \dot{M}_{acc} 's come from the modelling of the $H\alpha$ line profile in Natta et al. (2004). Therefore, the differences we observe between the \dot{M}_{acc} 's calculated from continuum excess and those de-

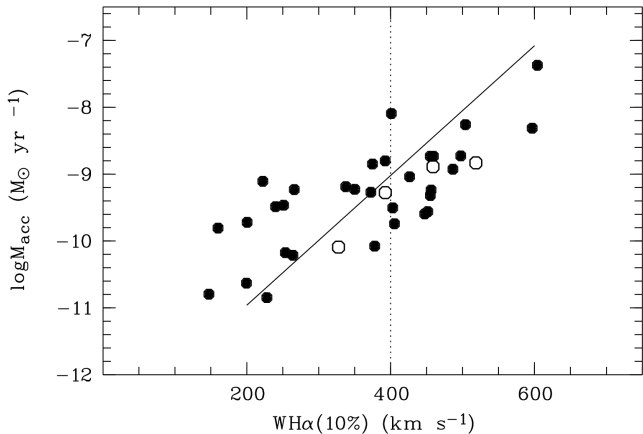


Fig. 9. The \dot{M}_{acc} vs. $\text{WH}\alpha(10\%)$ plot for the Lupus YSOs. Symbols are as in Figure 3. The $\text{WH}\alpha(10\%)$ measures are reported in Table 3. The \dot{M}_{acc} values of the sub-luminous objects were corrected, as discussed in Section 7.4. The continuous line represents the relationship $\log(\dot{M}_{\text{acc}}) = 9.7 \times 10^{-3} \cdot \text{WH}\alpha(10\%) - 12.89$ by (Natta et al. 2004).

rived from the Natta et al. (2004) relationship, can be attributed to the different methodologies adopted to measure \dot{M}_{acc} . In conclusion, although the $\text{H}\alpha$ line is the strongest in optical spectra of YSOs, special attention should be paid when using it to estimate mass accretion rates from the line width.

The least scattered $L_{\text{acc}}-L_{\text{line}}$ relations are those of the Balmer lines with $n>3$, the $\text{Br}\gamma$ line and the He I lines. The $\text{Pa}\beta$ and the $\text{Br}\gamma$ relations are recommended because these lines are the least affected from chromospheric emission. In contrast, the Ca II IRT relations are the most scattered. Even after correction for the photospheric absorption, the Ca II IRT relations appear more scattered than any of the Balmer lines, mainly because in some YSOs with very broad lines (e.g. Sz 83, Sz 72, Sz 69 and Lup 713) the blending with the $\text{Pa}13$, $\text{Pa}15$ and $\text{Pa}16$ lines contributes to the integrated flux, increasing the line luminosity. Without correction for the photospheric contribution the scatter in the Ca II IRT relations would be even larger. As in Mohanty et al. (2005), we also investigated relations between the surface flux of the Ca II IRT lines, $F_{\text{Ca II IRT}}$, and \dot{M}_{acc} , but the scatter remains rather large, on the order of 0.6 dex. In addition to the problem of blending with the Paschen lines, uncertainties in stellar radius and distance make the surface flux relations very scattered and uncertain. Moreover, no evidence is found in our data for a two-mode $F_{\text{Ca II IRT}}-\dot{M}_{\text{acc}}$ relation depending on the mass range, in contrast to the suggestion by Mohanty et al. (2005). This casts some doubts on whether the two Mohanty et al. (2005) relations may be produced by the different methodologies used to calculate \dot{M}_{acc} . In fact, the \dot{M}_{acc} values for six of the eight objects used by Mohanty et al. (2005) to derive the “low-mass” relation come from modelling of the $\text{H}\alpha$ line profile, while their “high-mass” relation is entirely based on veiling estimates. Note that Mohanty et al. (2005) briefly mention this as a possible reason for their different \dot{M}_{acc} ’s at their low and high mass regimes.

Another important aspect to be considered when determining accretion rates from emission lines and $L_{\text{acc}}-L_{\text{line}}$ relationships regards the contribution of chromospheric emission. The relative importance of (hydrogen) line emission with respect to L_{acc} is higher for small L_{acc} values, and chromospheric emission may be the dominant process in the lines. Based on the luminosity of several chromospheric emission lines in the Class-III templates, Manara et al. (2013a) determined a threshold below which chromospheric emission dominates line luminosities. The threshold depends on YSO effective temperature and age. Line luminosities yielding L_{acc} values below or just above that threshold should not be considered as accretion diagnostics.

Finally, as in Rigliaco et al. (2012), we stress that the average L_{acc} derived from several lines, measured simultaneously, has a much reduced error.

7.2. Discrepancies with magnetospheric accretion models

The most extensive calculations of line emission in the context of magnetospheric accretion models remain those of Muzerolle et al. (2001); they were performed for the stellar parameters typical of T Tauri stars ($M_{\star} = 0.5 M_{\odot}$, $R_{\star} = 2 R_{\odot}$), mass accretion rates between 10^{-6} and $10^{-9} M_{\odot}/\text{yr}$, different disc truncation radii and a wide range of gas temperatures. Their predictions of the dependence of the line luminosity and line ratios are at odds with the observed trends: namely, while the observed line luminosities increase roughly linearly with \dot{M}_{acc} , the models, which include constraints on the gas temperature, predict that the line luminosity will stay constant above $\dot{M}_{\text{acc}} \sim 10^{-8} M_{\odot}/\text{yr}$. Muzerolle et al. propose that the observations can only be understood if both \dot{M}_{acc} and the line fluxes are controlled by the size of the accretion flow, rather than reflecting the physical conditions of the accreting gas. In other words, if the flow occurs along discrete separate magnetic flux tubes, the gas physical conditions in each tube are similar, but the number of them can increase by an order of magnitude from object to object. We confirm the trend and show that it extends over a very large range of \dot{M}_{acc} .

The similarity of the physical conditions in the accreting gas for objects with very different \dot{M}_{acc} is suggested by a number of other properties as well. One is the fact that the hydrogen line ratios remain quite constant over a large range of \dot{M}_{acc} , and that there is no indication that optical depth effects play a significant role. See, e.g., the $\text{Pa}\beta/\text{Br}\gamma$ ratio in Figure 10: over a mass accretion range of 6 orders of magnitude, this ratio is constant within the uncertainties in the range 3–5, with no evidence for the lines to become optically thin at low \dot{M}_{acc} (e.g. Muzerolle et al. 2001). We note that in our sample there are no objects with $\text{Pa}\beta/\text{Br}\gamma} \sim 2$, as found in some ρ -Oph brown dwarfs by Gatti et al. (2006). It is possible that the physical conditions in the younger and brighter BDs in ρ -Oph differ from those in Lupus; however, it would be worthwhile to confirm the Gatti et al. (2006) results using spectra of the same quality of the ones used here.

Another indication for similar physical conditions in the accreting gas comes from considering the relations between L_{line} and L_{acc} derived in Section 5. To zero order they are linear, with slopes varying between 0.99 and 1.18 for the hydrogen Balmer, Paschen and Brackett lines, all equal

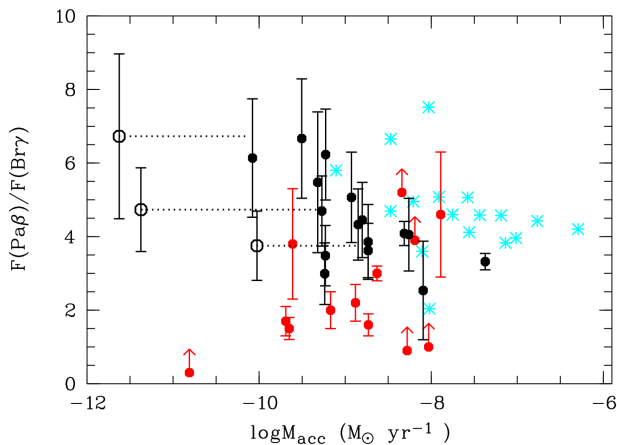


Fig. 10. The Pa β /Br γ ratio for the 19 YSOs in which both lines are detected (black dots and open circles). The shift in \dot{M}_{acc} to the right for the low-luminosity YSOs (open symbols), after correction for obscuration as explained in Section 7.4, is represented with the horizontal dotted lines. Objects in the ρ -Oph cloud studied by Gatti et al. (2006) are represented with red dots, while Taurus T Tauri stars from Muzerolle et al. (2001) are represented with cyan asterisks.

within the errors; similarly for the He I lines, with slopes in the range 0.90–1.16. This means that, over a range of L_{acc} of 5 orders of magnitude, a similar fraction of the accretion energy is emitted in each line, independently of their excitation potential and optical depth. Even if these fractions are in most cases very small (less than 1% in the case of the hydrogen lines and less than 0.1% for the He I lines, with only H α reaching $\sim 5\%$ of L_{acc}), they are surprisingly stable across the examined stellar parameters. This, again, suggests that the physical conditions of the accreting gas are very similar in all objects, and that only the covering factor changes from object to object.

To our knowledge, the suggestion by Muzerolle et al. (2001) that it is the geometry of the accretion flow that controls the rate at which the disc material accretes onto the central star has not been followed up by detailed models which include, for example, complex magnetic field configurations.

7.3. On the accretion properties of Lupus YSOs

Using simplified stellar evolution calculations for stars subject to time-dependent accretion, Tilling et al. (2008) conclude that the $L_{\text{acc}}-L_{\star}$ plane presents two main features namely, the $L_{\text{acc}} \approx L_{\star}$ upper boundary and diagonal tracks, which can be ascribed to accretion rates as the stars descend the Hayashi tracks. They show that the slope of such tracks on the $L_{\text{acc}}-L_{\star}$ plane is related to the power-law index of the \dot{M}_{acc} vs. age relationship. Our sample is consistent with a $L_{\text{acc}} \propto L_{\star}^{1.7}$ law, and under the Tilling et al. (2008) prescription, where $L_{\text{acc}} \propto L_{\star}^{(\eta-0.3)/0.7}$ (see their equation 12), this would mean $\eta = 1.5$, leading to $\dot{M}_{\text{acc}} \propto t^{-1.5}$.

A detailed observational study of the evolution of accretion requires complete and homogeneous samples of YSOs, with a diversity of ages, and well determined \dot{M}_{acc} (c.f. Sicilia-Aguilar et al. 2010). Gatti et al. (2008) find that

the accretion rates are significantly lower in σ -Ori than in younger regions, such as ρ -Oph, consistently with viscous disc evolution. Manara et al. (2012) and Rigliaco et al. (2011a) discussed the evolution of accretion as a function of stellar mass in the ONC and the σ -Ori cluster, respectively. The age range of our sample is too narrow to investigate in detail the $\dot{M}_{\text{acc}} \propto t^{-\eta}$ relation, but selecting the objects in the mass range $0.4M_{\odot}$ to $0.8M_{\odot}$, and excluding sub-luminous objects, an attempt to fit the relation yields $\eta = 1.3 \pm 0.3$, albeit with a large dispersion. The average \dot{M}_{acc} for objects in the same mass range is $1.3^{(+1.9)}_{(-0.8)} \times 10^{-9} M_{\odot} \text{ yr}^{-1}$, which is consistent with the calculations of the evolution of viscous discs for $0.5 M_{\odot}$ YSOs by Hartmann et al. (1998) at 3 Myr (see their Figure 3). To investigate empirically the \dot{M}_{acc} vs. age relationship, Caratti o Garatti et al. (2012) normalised the \dot{M}_{acc} to M_{\star}^2 in order to account for the dependence of \dot{M}_{acc} on mass. Following this approach for the Lupus YSOs, some number statistics is gained by including in the fit YSOs with mass up to $\sim 1 M_{\odot}$. Although the dispersion is slightly reduced, the result is practically identical.

Since the stellar mass undergoes negligible changes during the Class-II phase, the \dot{M}_{acc} vs. M_{\star} relation represents a diagnostic tool for the evolution of \dot{M}_{acc} (Clarke & Pringle 2006). From the theoretical point of view, it has been suggested by Vorobyov & Basu (2008) that the $\dot{M}_{\text{acc}} \propto M_{\star}^2$ relationship can be explained on the basis of self-regulated accretion by gravitational torques in self-gravitating discs. These authors argue that the relationship can be better described as a double power-law, with the break occurring at $M_{\star} \approx 0.25 M_{\odot}$, rather than a function with a single exponent (Vorobyov & Basu 2009). Interestingly, such kink occurs close to the value of mass where the techniques to calculate \dot{M}_{acc} differ. Thus, they also point out the different techniques used to determine \dot{M}_{acc} as a possible cause for the apparent bi-modal power-law.

The power-law index of the $\dot{M}_{\text{acc}}-M_{\star}$ relation for Lupus is also ~ 2 , but the scatter is smaller than in previous data sets (c.f. the standard deviation for the Lupus fit is a factor 2 less than for the Taurus sample in Herczeg & Hillenbrand 2008). As pointed out in Section 2, our sample represents about 50% of the complete population of Class-II YSOs in the Lupus-I and Lupus-III clouds. It is thus rather unlikely that the large range of \dot{M}_{acc} (> 2 dex) at a given mass observed in other data sets will show-up also in Lupus, if a more complete sample is investigated. However, it would be worthwhile to study the YSOs more massive than those in our sample, using spectra of the same quality as here. In addition, although our number statistics is low, there is no evidence for a double power-law in our sample, supporting the conclusion that the apparent bi-modal relations suggested in the literature between \dot{M}_{acc} and other YSOs properties are probably the result of mixing up \dot{M}_{acc} 's derived with different methods.

7.4. The sub-luminous YSOs: evolution or edge-on discs ?

The underluminosity and strong emission lines in the optical spectrum of Par-Lup3-4 were first discussed by Comerón et al. (2003), who found difficult explaining their observations in terms of either a photospheric continuum suppressed by an edge-on disc or an embedded source seen in

scattered light. They favor instead the scenario in which the PMS evolution is significantly modified by the accretion process, as suggested in Baraffe & Chabrier (2010). The analysis of the SED resulting in a disc inclination angle of $\sim 81^\circ$ (Huelamo et al. 2010) and the tiny difference in velocity between the red-shifted and blue-shifted components of the outflow (Bacciotti et al. 2011; Whelan et al. 2013) provide evidence that we are seeing the Par-Lup3-4 disc almost edge-on. However, as in Comerón et al. (2003), strong Ca II IRT lines are also detected in our X-Shooter spectrum, meaning that not all the emission from the accretion-flows in the inner regions is suppressed by the optically thick disc.

Comerón et al. (2003) also pointed out Sz 106 and Sz 113 as underluminous, although not so extreme. Underluminosity is confirmed here for Sz 106, while no evidence for such phenomenon is observed in Sz 113⁹. We also find Lup 706 and Sz 123B underluminous, but not as much as Par-Lup3-4.

As examined by Baraffe & Chabrier (2010), episodic strong accretion during PMS evolution of low-mass stars produces objects with smaller radius, higher central temperature, and lower luminosity compared to the non-accreting counterpart of the same mass and age, resulting in low-luminosity objects. Should the PMS evolution of the 4 sub-luminous YSOs have been significantly altered by episodic strong accretion, their surface gravity should also appear larger than for objects of the same mass and age. One way to test this possibility is through independent estimates of the surface gravity. We have done such estimates while correcting the photospheric contribution of the Na I D and Ca II IRT lines (see Section 4.4), when using the gravity sensitive Na I ($\lambda\lambda 818.3 \text{ nm}/819.48 \text{ nm}$) and the K I ($\lambda\lambda 766.50 \text{ nm}/769.90 \text{ nm}$) doublets (see Stelzer et al. 2013b, for the method), for which veiling is negligible in these objects. The results of the analysis yield $\log g$ values (3.5, 3.7, 4.3, and 3.9 for Par-Lup3-4, Lup 706, Sz 106 and Sz 123B, respectively) that are very similar as for the other YSOs in the sample, and lower than those expected for apparently more evolved objects. Hence, we reject the hypothesis that underluminosity of these objects is the result of modified PMS evolution by accretion episodes.

The scatter in several plots shown throughout the previous sections is significantly reduced when L_{acc} is normalised to the YSOs luminosity; the L_{acc}/L_\star values of the sub-luminous objects are consistent with those for the other YSOs, suggesting that some process is in act that affects L_{acc} and L_\star in the same way. As in the case of Par-Lup3-4, such a process may be gray circumstellar extinction. In the magnetospheric accretion model, the line and accretion luminosities originate in the inner parts of the star-disc system. Thus, under the assumption of gray circumstellar extinction due to disc obscuration both L_{acc} and L_{line} , as well as the YSO luminosity are dimmed by the same amount, which depends on disc inclination angle, disc flaring, and dust opacity. The effect thus cancels out when considering the L_{acc}/L_\star ratio and has no consequences on the L_{acc} vs.

L_{line} relationships, but may have an important impact on the \dot{M}_{acc} determinations for the most obscured objects.

Under the hypothesis of a gray obscuration, it can be inferred from Figure 3 that the "obscuration factors" by which the luminosity of the four objects should be multiplied to fit the average trend of the mass-luminosity relationship are ~ 25 , 10, 6, and 4 for Par-Lup3-4, Lup706, Sz 123B, and Sz 106, respectively. At a fixed mass, Equation 1 implies $\dot{M}_{\text{acc}} \propto L_{\text{acc}} \cdot L_\star^{0.5}$, because the YSO radius scales with the square root of the luminosity. Assuming that the obscuration factor suppresses both L_{acc} and L_\star by the same amount, the \dot{M}_{acc} values for the low-luminosity YSOs can be corrected as $\dot{M}_{\text{acc}}(\text{corrected}) = (\text{obscuration factor})^{1.5} \cdot \dot{M}_{\text{acc}}$. When the obscuration factors are applied to L_\star , L_{acc} and \dot{M}_{acc} , the four underluminous objects behave exactly as the other YSOs in the various plots. Detailed analysis of the spectral energy distribution of these YSOs is required to constrain the geometry of their disc.

8. Summary and conclusions

Our study with X-Shooter@VLT is the first presenting UV-excess measures of accretion luminosity, simultaneously to intermediate-resolution spectroscopy of a large number of emission line diagnostics, from $\sim 330 \text{ nm}$ to 2500 nm , in a significant and homogeneous sample of very low-mass young stellar and sub-stellar objects in Lupus. The quality of the spectra and the accuracy in flux calibration, both in the continuum and the lines, allowed the characterisation of the sample and the computation of L_{acc} vs. L_{line} relations for an unprecedentedly large number (39) of emission line diagnostics, as well as to study the accretion properties of the sample. The main results are summarised here.

The accretion emission in our sample is dominated by continuum emission in the Balmer and Paschen continuum. For the vast majority of the YSOs the integrated line luminosity totals less than one third of L_{acc} . Most of the line luminosity is due to Balmer lines, yet the contribution of the Paschen, Brackett and other permitted lines in the strongest accretors may be comparable to the total Balmer line luminosity. The accretion level of all the YSOs studied here is well above the expected chromospheric contribution, even at the lowest values of L_{acc} .

The 39 empirical L_{acc} vs. L_{line} relationships computed here have in general a lower dispersion as compared to previous relationships in the literature. Our L_{acc} vs. L_{line} relationships are in good agreement with previous results, but systematic differences may exist at different mass regimes with respect to studies adopting other methodologies to measure L_{acc} or \dot{M}_{acc} . We confirm that for low-mass YSOs ($M_\star < 0.3 M_\odot$), H α line profile modelling may underestimate \dot{M}_{acc} by 0.6 to 0.8 dex with respect to \dot{M}_{acc} derived from continuum-excess measures.

The least scattered among our $L_{\text{acc}}-L_{\text{line}}$ relationships are those for the Balmer lines $n > 3$, the Br γ line and the He I lines. The Pa β and the Br γ relations are recommended because less affected by chromospheric activity than the optical lines. The most scattered relations are those of the Ca II IRT. Likewise, the Ca II IRT surface-flux relationships have large scatter (~ 0.6 dex), mainly due to the blending and contribution of Paschen lines in strong accretors and to the uncertainties on stellar parameters. The previously sug-

⁹ We noted some differences between our spectra of Sz 106 and Sz 113 and those published by Comerón et al. (2003). For instance, the H α equivalent width we measure for Sz 106 is 11.6 \AA while Comerón et al. (2003) claim more than 100 \AA . Also, lots of forbidden lines are seen in our spectrum of Sz 113, while Comerón et al. (2003) detect none. Note, however, that the Comerón et al. (2003) spectra have much lower resolution than ours.

gested bi-modality with respect to the mass of the Ca II IRT surface-flux relationships is most likely induced by the mix of different methodologies to derive \dot{M}_{acc} . More generally, we conclude that mixing mass-accretion rates calculated with different techniques may lead to a spurious bi-modality in the relationships between \dot{M}_{acc} and YSOs properties. The average L_{acc} derived from several lines, measured simultaneously, has a significantly reduced error.

The accretion properties of the YSOs studied here are similar to those of other low-mass YSOs in regions like Taurus, ρ -Oph or σ -Ori. We derive \dot{M}_{acc} in the range from 2×10^{-12} to $4 \times 10^{-8} M_{\odot} \text{ yr}^{-1}$ for objects with masses from 0.03 to $1.2 M_{\odot}$. We conclude that $\dot{M}_{\text{acc}} \propto M_{\star}^{1.8(\pm 0.2)}$ for the Lupus sample studied here, in agreement with most studies of the $\dot{M}_{\text{acc}} - M_{\star}$ relationship. The scatter for the Lupus relationship is smaller than for other data sets. The average \dot{M}_{acc} for objects with mass between 0.4 and $0.8 M_{\odot}$ is consistent with the calculations of the evolution of \dot{M}_{acc} in viscous discs for 3 Myr old objects with $0.5 M_{\odot}$ (Hartmann et al. 1998).

We confirm, and extend over more than 5 orders of magnitude in \dot{M}_{acc} , some properties of the accretion emission, already known for a more limited range of \dot{M}_{acc} . In particular, that line ratios, as well as the fraction of L_{acc} emitted in each line, are roughly independent of \dot{M}_{acc} , and that the line luminosities increase almost linearly with \dot{M}_{acc} over the whole range. This suggests that some inconsistencies between magnetospheric accretion models and observations still prevail, but a number of properties (e.g. constant hydrogen line ratios, same accretion budget emitted in each line independently of optical depth, and linear correlation of the line luminosity with \dot{M}_{acc} , among other) suggest that the physical conditions of the accreting gas, over a large range of \dot{M}_{acc} , are similar. Our data show that this properties are valid over a large range in \dot{M}_{acc} , extending down to the very low-mass regime. We thus confirm the suggestion by Muzerolle et al. (2001) that it is the geometry of the accretion flows that controls the rate at which the disc material accretes onto the central star: larger mass accretion rates require larger emitting areas. Detailed magnetospheric accretion models, incorporating complex magnetic field topologies, are needed to understand whether other physical parameters (e.g. magnetic field topology) play a role in the accretion physics.

Acknowledgements. We thank the anonymous referee for her/his careful reading and for suggestions. JMA, EC, BS, and KB thank G. Attusino for stimulating discussions. We also thank B. Nisini, T. Giannini and S. Antoniucci for lively discussions. We thank V. D’Odorico, P. Goldoni and A. Modigliani for their help with the X-Shooter pipeline, and F. Getman and G. Capasso for the installation of the different pipeline versions at Capodimonte. We also thank the ESO staff, in particular F. Patat for suggestions in OB preparation and C. Martayan for support during the observations. Financial support from INAF is also acknowledged. This research made use of the SIMBAD database, operated at the CDS (Strasbourg, France). This publication makes use of data products from the Two Micron All Sky Survey, which is a joint project of the University of Massachusetts and the Infrared Processing and Analysis Center/California Institute of Technology, funded by NASA and the National Science Foundation. This publication makes use of data products from the Wide-field Infrared Survey Explorer, which is a joint project of the University of California, Los Angeles, and the Jet Propulsion Laboratory/California Institute of Technology, funded by the National Aeronautics and Space Administration.

References

- Alcalá, J. M., Stelzer, B., Covino, E., et al. 2011, AN, 332, 242
 Alexander, R. D., Clarke, C. J., & Pringle, J. E. 2006, MNRAS, 369, 216
 Allard, F., Homeier, D., & Freytag, B. 2010, ArXiv 1011.5405
 Allen, P. R., Luhman, K. L., Myers, P. C., et al. 2007, ApJ, 655, 1095
 Allers K.N., Kessler-Silacci J.E., Cieza L.A. & Jaffe D.T. 2006, ApJ, 644, 364
 Antonucci, S., Garcia Lopez, R., Nisini, B., et al. 2011, A&A, 534, 32
 Appenzeller, I., Jankovics, I., & Krautter, J. 1983, A&AS, 53, 291
 Baraffe, I., Chabrier, G., Allard, F., et al. 1998, A&A, 337, 403
 Baraffe, I., & Chabrier, G. 2010, A&A, 521, 44
 Bacciotti, F., Whelan, E. T., Alcalá, J. M., et al. 2011, ApJ, 737, 26
 Bayo, A., Barrado, D., Huéramo, N., Morales-Calderón, M., et al. 2012, A&A, 547, 80
 Biazzo, K., Alcalá, J. M., Covino, et al. 2012, A&A, 547, 104
 Calvet, N., & Gullbring, E. 1998, ApJ, 509, 802
 Calvet, N., Hartmann, L., & Strom, S. E. 2000, in Protostars and Planets IV, 377
 Calvet, N., Muzerolle, J., Briceño, C., et al. 2004, AJ, 128, 1294
 Caratti o Garatti, A., García López, R., Antoniucci, S., et al. 2012, A&A, 538, 64
 Chabrier, G., Baraffe, I., Allard, F., & Hauschildt, P. 2000, ApJ, 542, 464
 Clarke, C. J., & Pringle, J. E. 2006, MNRAS, 370, L10
 Comerón, F., Fernández, M., Baraffe, I., Neuhäuser, R., & Kaas, A. 2003, A&A, 406, 1001
 Comerón, F., Spezzi, L., & López-Martí, B. 2009, A&A, 500, 1045
 Comerón, F. 2008 in Handbook of Star Forming Regions, Volume II: The Southern Sky ASP Monograph Publications, Vol. 5, Edited by Bo Reipurth, p. 295
 Comerón, F., Testi, L., & Natta, A. 2010, A&A, 522, 47
 Costigan, G., Scholz, A., Stelzer, B., et al. 2012, MNRAS, 427, 1344
 Costigan, G., Vink, J. S., Scholz, A., Ray, T., & Testi, L. 2013, MNRAS, submitted
 Cutri, R. M., et al. 2003, 2MASS All Sky Catalog of Point Sources, The IRSA 2MASS All-Sky Point Source Catalog, NASA/IPAC Infrared Science Archive (Pasadena, CA: NASA/IPAC), <http://irsa.ipac.caltech.edu/application/Gator>
 D’Antona, & F., Mazzitelli, I. 1997, Mem.SAIt., 68, 807
 Draine, B. T. 2003, ARA&A, 41, 241
 Dullemond, C. P., & Dominik, C. 2004, A&Ap, 417, 159
 Edwards, S., Fischer, W., Hillenbrand, L., & Kwan, J. 2006, ApJ, 646, 319
 Evans, N.J., II, Dunham, M. M., Jørgensen, J. K.; Enoch, M. L., et al. 2009, ApJS, 181, 321
 Fang, M., van Boekel, R., Wang, W., et al. 2009, A&A, 504, 461
 Fang, M., Jinyoung, S., van Boekel, R., et al. 2013, ApJS, 207, 5
 Feigelson, E. D., & Nelson, P. I. 1985, ApJ, 293, 192
 Fernández, M. & Comerón, F. 2001, A&A, 380, 264
 Frasca, A., Guillout, P., Marilli, E., et al. 2006, A&A, 454, 301
 Gahm, G. F., Walter, F. M., Stempels, H. C., Petrov, P. P., & Herczeg, G., 2008, A&A, 482, 35
 Gatti, T., Testi, L., Natta, A., et al. 2006, A&A, 460, 547
 Gatti, T., Natta, A., Randich, S., et al. 2008, A&A, 481, 423
 Giannini, T. et al. 2013, submitted
 Gorti, U., & Hollenbach, D. 2009, ApJ, 690, 1539
 Graham, J. A. & Heyer, M. H. 1988, PASP, 100, 1529
 Gullbring, E., Hartmann, L., Briceño, C., & Calvet, N. 1998, ApJ, 492, 323
 Guenther, E. W., Esposito, M., Mundt, R., Covino, E., Alcalá, J. M., et al. 2007, A&A, 467, 1147
 Hartigan, P., Kenyon, S. J., Hartmann, L., et al. 1991, ApJ, 382, 617
 Hartigan, P., & Kenyon, S. J. 2003, ApJ, 583, 334
 Hamann, F., & Persson, S. E. 1992, ApJS, 82, 247
 Hartmann, L. E., Hewett, R., & Calvet, N. 1994, ApJ, 426, 669
 Hartmann, L. E., "Accretion Processes in Star Formation" Cambridge Univ. Press.
 Hartmann, L. E., Calvet, N., Gullbring, E., & D’Alessio, P. 1998 ApJ, 495, 385
 Hauschildt, P., Allard, F., & Baron, E. 1999a, ApJ, 512, 277
 Hauschildt, P., Allard, F., Ferguson, J., et al. 1999b, ApJ, 525, 871
 Herbig, G. H., & Soderblom, D. R., 1980 ApJ, 242, 628
 Herczeg, G., & Hillenbrand, L. A. 2008, ApJ, 681, 594
 Herczeg, G., Cruz, K. L., & Hillenbrand, L. A. 2009, ApJ, 696, 1589
 Herczeg, G., Linsky, J., Valenti, J., et al. 2002, ApJ, 572, 310

- Herczeg, G., Walter, F. M., Linsky, J. L., et al. 2005, *AJ*, 129, 2777
- Huélamo, N., Bouy, H., Pinte, C., et al. 2010, *A&A*, 523, 42
- Hughes, J., Hartigan, P., Krautter, J., & Kelemen, J. 1994, *AJ*, 108, 1071
- Ingleby, L., Calvet, N., Bergin, E., et al. 2011, *ApJ*, 743, 105
- Ingleby, L., Calvet, N., Herczeg, G., et al. 2013, *ApJ*, 767, 112
- Johns-Krull, C. M. 2007, *ApJ*, 664, 975
- Kenyon, S., & Hartmann, L. 1987, *ApJ* 323, 714
- Kenyon, S. & Hartmann, L. 1995, *ApJ*, 101, 117
- Königl, A. 1991, *ApJ*, 370, L39
- Kurosawa, R., Harries, T. J., & Symington, N. H. 2006, *MNRAS*, 370, 580
- López-Martí, B., Eisloffel, J., & Mundt, R., *A&A*, 440, 139
- Luhman, K. L., Stauffer, J., Muench, A., et al. 2003, *ApJ*, 593, 1093
- Luhman, K., Adame, L., D'Alessio, P., Calvet, N., Hartmann, L., et al. 2005, *ApJ*, 635, 93
- Lynden-Bell, D., & Pringle, J. E. 1974, *MNRAS*, 168, 603
- Manara, C. F., Robberto, M., Da Rio, N., et al. 2012, *ApJ*, 755, 154
- Manara, C., Testi, L., Rigliaco, E., et al. 2013a, *A&A*, 551, 107
- Manara, C., Beccari, G., Da Rio, N., De Marchi, G., Natta, A., et al. 2013b, *A&A*, in press (arXiv1307.8118)
- Melo, C. 2003, *A&A*, 410, 269
- Merín, B., Jørgensen, J.K., Spezzi, L., et al. 2008, *ApJS*, 177, 551
- Modigliani, A., Goldoni, P., Royer, F., et al. 2010, in *Observatory Operations: Strategies, Processes, and Systems III*, SPIE, Vol. 7737, eds. D. R. Silva, A. B. Peck, & B. T. Soifer
- Mohanty, S., Jayawardhana, R., & Basri, G. 2005, *ApJ*, 626, 498
- Mohanty, S., Greaves, J., Mortlock, D., Pascucci, I., Scholz, A., et al. 2013, *ApJ*, in press
- Mortier, A., Oliveira, I., & van Dishoeck, E. F. 2011, *MNRAS*, 418, 1194
- Muzerolle, J., Hartmann, L., & Calvet, N. 1998, *AJ*, 116, 455
- Muzerolle, J., Calvet, N., Briceño, C., Hartmann, L., & Hillenbrand, L. 2000, *ApJL*, 535, 47
- Muzerolle, J., Calvet, N., & Hartmann, L. 2001, *ApJ*, 550, 944
- Muzerolle, J., Hillenbrand, L., Calvet, N., et al. 2003, *ApJ*, 592, 266
- Muzerolle, J., Luhman, K., Briceño, C., et al. 2005, *ApJ*, 625, 906
- Natta, A., Testi, L., Muzerolle, J., et al. 2004, *A&A*, 424, 603
- Natta, A., Testi, L., & Randich, S. 2006, *A&A*, 452, 245
- Nisini, B., Bacciotti, F., Giannini, et al. 2005, *A&A*, 441, 159
- Olofsson, J., Augereau, J.-C., van Dishoeck, E. F., Merín, B., Grosso, N., et al. 2010, *A&A*, 520, 390
- Olofsson, J., Szucs, L., Henning, Th., Linz, H., Pascucci, I., Joergens, V. 2013, arXiv1310.0834
- Paatz, G., & Camenzind, M. 1996, *A&A*, 308, 77
- Pinte, C., Padgett, D. L., Ménard, F., et al. 2008, *A&Ap*, 489, 633
- Pringle, J. E. 1991, *MNRAS*, 248, 754
- Rajpurohit, A. S., Reylé, C., Allard, F., Homeier, D., Schultheis, M. et al. 2013, *A&A*, 556, 15
- Reipurth, B., Bally, J., Graham, J. A., et al. 1986, *A&A*, 164, 51
- Ricci, L., Testi, L., Natta, A., et al. 2010, *A&Ap*, 512, 15
- Riddick, F., Roche, P., & Lucas, P. 2007, *MNRAS*, 381, 1067
- Rigliaco, E., Natta, A., Randich, S., et al. 2011a, *A&A*, 525, 47
- Rigliaco, E., Natta, A., Randich, S., et al. 2011b, *A&A*, 526, 6
- Rigliaco, E., Natta, A., Testi, L., et al. 2011c, *AN*, 332, 249
- Rigliaco, E., Natta, A., Testi, L., et al. 2012, *A&A*, 548, 56
- Rygl, K. L. J., Benedettini, M., Schisano, E., Elia, D., Molinari, S., et al. 2013, *A&A*, 549, 1
- Rojas-Ayala, B., Covey, K. R., Muirhead, P. S., & Lloyd, J. P. 2012, *ApJ*, 748, 93
- Scholz, A., Jayawardhana, R., Wood, K., Meeus, G., Stelzer, B., et al. 2007, *ApJ*, 660, 1517
- Sicilia-Aguilar, A., Henning, Th., & Hartmann, L. W. 2010, *ApJ*, 710, 597
- Shu, F., Najita, J., Ostriker, E., & Wilkin, F. 1994, *ApJ*, 429, 781
- Spezzi, L., Alcalá, J. M., Covino, E., et al. 2008, *ApJ*, 680, 1295
- Stelzer, B., Alcalá, J. M., Biazzo, K., et al. 2012, *A&A*, 537, 94
- Stelzer, B., Alcalá, J. M., Scholz, A., et al. 2013a, *A&A*, 551, 106
- Stelzer, B., Frasca, A., Alcalá, J.M., et al. 2013b, *A&A*, in press (arXiv1308.5563)
- Testi, L. 2009, *A&A*, 503, 639
- Tilling, I., Clarke, C. J., Pringle, J. E., & Tout, C. A. 2008, *MNRAS*, 385, 1530
- Uchida, Y. & Shibata, K. 1985, *PASJ*, 37, 515
- Valenti, J. A., Basri, G., & Johns, C. M. 1993, *ApJ*, 106, 2024
- Vernet, J., Dekker, H., D'Odorico, S., Kaper, L., et al. 2011, *A&A*, 536, 105
- Vorovyov, E. J., & Basu, S. 2008, *ApJ*, 676, 139
- Vorovyov, E. J., & Basu, S. 2009, *ApJ*, 703, 922
- Weingartner, J. C., Draine, B. T. 2001, *ApJ*, 548, 296
- Whelan, E., Bonito, R., Antonucci, S., et al. 2013, *A&A*, submitted
- White, R., & Hillenbrand, L. A. 2004, *ApJ*, 582, 1109
- White, R. & Basri, G. 2003, *ApJ*, 582, 1109
- Wichmann, R., Krautter, J., Covino, E., et al. 1997, *A&A*, 320, 185
- Wright, E. L., Eisenhardt, P. R. M., Mainzer, A. K., Ressler, M. E., Cutri, R. M. et al. 2010, *AJ*, 140, 1868
- Yang, H., Herczeg, G., Linsky, J., et al. 2012, *ApJ*, 744, 121

Appendix A: Correction for telluric bands

The flux calibrated one-dimensional spectra resulting from the X-Shooter pipeline or our MIDAS procedure are not corrected for the contribution of telluric bands. Therefore, the telluric standards were used to perform the correction using the IRAF task "telluric". The procedure basically consists on dividing the target spectrum by the telluric spectrum multiplied by an appropriate scaling factor. This factor depends on the ratio of the airmass of the target and the telluric standard. Since the targets and their assigned telluric standards were observed at very similar air-masses in most cases, such factor is normally close to one. The procedure was applied independently in the VIS and NIR spectra, in a different way.

A.1. Telluric correction in the VIS spectra

The correction was done directly on the one-dimensional flux calibrated VIS spectra of the targets using the assigned tellurics. However, in order to avoid the introduction of the spectral energy distribution of the telluric on the flux calibrated spectra, the tellurics were first normalized to their continuum and their hydrogen lines and other stellar lines were removed by fitting combinations of Gaussian, Lorentzian and Voigt functions. The resulting normalised telluric spectra, free of photospheric lines were then used as input in the IRAF task "telluric". In Figure A.1 left panels examples of the telluric correction in the spectral range of the $K\text{I } \lambda\lambda 766.49, 769.90$ nm and the $\text{Na I } \lambda\lambda 818.33, 819.481$ nm doublets are shown.

A.2. Telluric correction in the NIR spectra

For the NIR spectra, a pseudo-response function was first derived by dividing the non flux-calibrated telluric by a black-body of the same effective temperature as the telluric. Such pseudo-response function was also cleaned for photospheric lines in the same way as in the VIS. The resulting pseudo-response function, free of stellar lines and containing the telluric bands, was then used as input in the IRAF task "telluric". Note that the target spectrum to be used as input of the IRAF task was the non-flux calibrated one-dimensional spectrum. In this way, the telluric correction and the correction for the response function were done simultaneously in the NIR. Although the shape of the resulting spectrum after this procedure is correct, the flux calibration is only relative to the pseudo-response function. Therefore, a factor was applied in order to bring the NIR spectrum to the absolute flux scale. Such factor was estimated using the non-telluric corrected, but flux-calibrated spectra resulting from both the X-Shooter pipeline and our MIDAS procedure. In Figure A.2 examples of the telluric correction of the YSO Lup713 are shown in two spectral ranges of the NIR arm. Note that in the range 2000-2140 nm the pipeline yields a bump with respect to the telluric corrected spectrum. This defect in the latter is corrected because the pseudo-response function contains such bump.

Appendix B: Impact of veiling on spectral typing and extinction

B.1. Veiling and spectral indices

Strong veiling may influence the spectral indices used to classify the M-type YSOs. To investigate the impact of veiling on the spectral indices, we proceed as follows. A constant veiling was artificially added to the spectra of the Class-III templates in the spectral range between 740 nm and 860 nm, where the indices are computed. Then, the new indices and spectral type of the "veiled" spectrum were derived. The

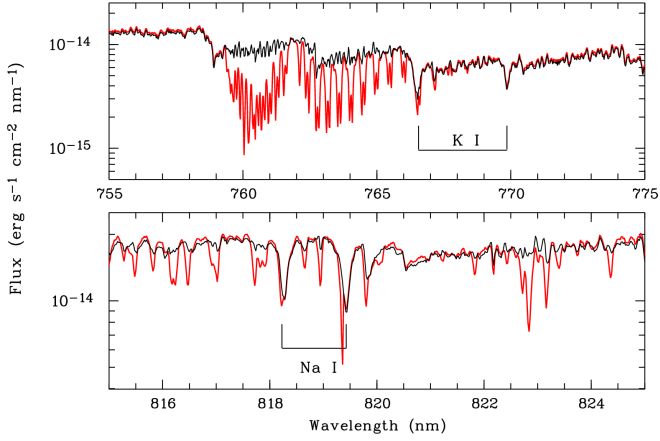


Fig. A.1. Example of telluric-corrected spectrum (black lines) of the YSO Lup713 in the range of the K I $\lambda\lambda$ 766.49, 769.90 nm (upper panel) and the Na I $\lambda\lambda$ 818.33, 819.48 nm (lower panel) doublets. The non-corrected spectra are overlaid with red lines.

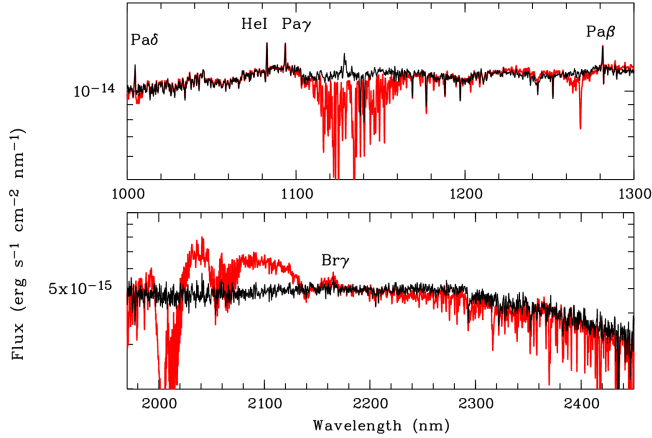


Fig. A.2. Examples of the telluric corrected spectrum of Lup713 in two spectral ranges of the NIR arm. The non-corrected spectra are overlaid with red lines in both panels.

effect of veiling is to yield systematically earlier types, but in that spectral range it should be greater than one in order to induce a difference of about one spectral sub-class. As seen in Section 4.1.1, the strongest veiling, at ~ 710 nm, among the M-type YSOs is less than 0.6 and corresponds to Sz 113. For this object we estimate that veiling would introduce an uncertainty of 0.4 sub-class in spectral type. For the other YSOs excess emission in the Paschen continuum is smaller (see Table 3). For all the M-type YSOs veiling is estimated to influence the spectral type classification to less than 0.3 spectral sub-classes.

B.2. Veiling and extinction

The effect of strong veiling is to make YSOs objects intrinsically bluer than the templates we use to derive extinction. Thus, our method may underestimate extinction if veiling is very strong. To investigate by how much, we proceed as follows. The observed spectrum of a given YSO, $F_{YSO}(\lambda)$, is the sum of the flux of the object, $F_*(\lambda)$, plus the flux of the continuum excess emission, $F_{cont}(\lambda)$, extinguished with an extinction law, A_λ/A_V . So the flux we observe is $F_{YSO}(\lambda) = (F_*(\lambda) + F_{cont}(\lambda)) \cdot e^{-0.4 \cdot (A_\lambda/A_V) \cdot A_V}$. In order to get the extinction,

free of veiling effects, we must apply our methods, not to $F_{YSO}(\lambda)$, but to the de-veiled spectrum:

$$F_{YSO}(\lambda) - F_{cont}(\lambda) \cdot e^{-0.4 \cdot (A_\lambda/A_V) \cdot A_V} \quad (\text{B.1})$$

We can assume that the continuum flux is the model continuum excess emission derived in Section 4.1.1, hence from Equation B.1 we can compute a "de-veiled" spectrum, provided we know A_V . Since we do not know A_V in advance, we proceed in a two-step fitting procedure. As first guess of A_V we use the value derived from our template fitting procedure applied to $F_{YSO}(\lambda)$, and compute an de-veiled spectrum using Equation B.1. A new A_V is then derived from our fitting procedure applied to the first de-veiled spectrum. This spectrum is used to compute a new A_V value and to redden the $F_{cont}(\lambda)$ to be used again to calculate a second de-veiled spectrum, and so on until a A_V value is found which leads to the best match with the template.

In practice, we use as a test case Sz 113, the most veiled M-Type YSO in our sample. The extinction we derive as "first guess" is 1 mag. Thus, the model continuum excess emission derived in Section 4.1.1 was reddened at extinctions between 1 mag and 2 mag in steps of 0.25 mag. The results were then subtracted to the observed spectrum of Sz 113. The several de-veiled spectra were then processed with our fitting procedure. The best compromise between reddened model continuum and de-reddened de-veiled spectra occurs at $A_V = 1.5$ mag. We conclude that for our most veiled M-Type YSO extinction is underestimated by less than 0.5 mag.

Appendix C: On-line material

Table C.1. Ancillary optical and near-IR photometry

Object	B (mag)	V (mag)	R (mag)	I (mag)	Z (mag)	J (mag)	H (mag)	K (mag)
Sz66	16.45±0.01	15.00±0.01	14.51±0.01	12.56±0.01	11.53±0.02	10.89±0.03	9.88±0.03	9.29±0.03
AkC2006-19	18.38±0.05	17.74±0.01	17.04±0.01	14.91±0.01	14.09±0.01	12.98±0.02	12.41±0.02	12.13±0.02
Sz69	17.41±0.06	16.25±0.06	14.84±0.01	13.63±0.01	12.28±0.01	11.18±0.03	10.16±0.03	9.41±0.03
Sz71	13.80±0.01	13.54±0.01	13.70±0.01	11.83±0.01	11.28±0.02	10.07±0.02	9.18±0.02	8.63±0.02
Sz72	15.96±0.01	14.79±0.01	13.55±0.02	12.25±0.02	...	10.57±0.03	9.77±0.03	9.33±0.02
Sz73	18.21±0.04	16.37±0.02	14.90±0.02	13.44±0.01	...	10.74±0.03	9.53±0.03	8.83±0.02
Sz74	15.96±0.02	14.18±0.01	12.98±0.02	11.44±0.01	...	9.23±0.02	8.10±0.02	7.43±0.02
Sz83	11.70±0.01	11.40±0.01	10.63±0.02	9.84±0.02	...	8.73±0.03	7.82±0.04	7.14±0.02
Sz84	17.54±0.03	16.16±0.01	14.53±0.04	12.94±0.02	...	10.93±0.02	10.20±0.02	9.85±0.03
Sz130	15.82±0.05	14.71±0.05	13.56±0.54	12.46±0.01	12.26±0.02	10.73±0.05	9.93±0.05	9.62±0.05
Sz88A (SW)	13.67±0.01	13.02±0.01	13.06±0.01	11.91±0.01	11.21±0.01	10.20±0.03	9.36±0.03	8.76±0.02
Sz88B (NE)	17.17±0.01	15.72±0.01	15.32±0.01	13.33±0.01	12.57±0.01	11.53±0.03	10.87±0.03	10.51±0.02
Sz91	16.25±0.05	14.58±0.05	14.38±0.01	12.92±0.01	12.25±0.01	11.06±0.02	10.12±0.02	9.85±0.02
Lup713	18.38±0.05	...	17.77±0.02	15.68±0.02	14.06±0.01	13.24±0.03	12.57±0.03	12.13±0.03
Lup604s	16.94±0.05	17.01±0.05	16.51±0.01	14.31±0.01	13.34±0.01	12.15±0.03	11.45±0.03	11.07±0.02
Sz97	16.18±0.05	14.61±0.05	14.77±0.01	12.92±0.01	12.24±0.01	11.24±0.02	10.55±0.02	10.22±0.02
Sz99	15.49±0.05	16.0 ±0.05	15.74±0.01	14.17±0.01	13.28±0.01	11.93±0.02	11.21±0.02	10.75±0.02
Sz100	16.62±0.05	15.43±0.05	15.22±0.01	13.12±0.01	12.18±0.01	10.98±0.02	10.35±0.02	9.91±0.02
Sz103	...	11.14±0.05	15.18±0.01	13.15±0.01	12.40±0.01	11.38±0.02	10.62±0.02	10.23±0.02
Sz104	...	15.25±0.05	15.64±0.01	13.57±0.01	12.78±0.01	11.66±0.02	11.00±0.02	10.65±0.02
Lup706	...	20.70±0.06	18.44±0.05	16.68±0.03	16.68±0.03	15.17±0.06	14.24±0.06	13.83±0.04
Sz106	17.63±0.05	16.26±0.02	15.97±0.02	14.66±0.01	14.14±0.01	11.65±0.03	10.66±0.03	10.15±0.02
Par-Lup3-3	16.76±0.05	...	16.27±0.01	14.24±0.01	13.19±0.01	11.45±0.02	10.17±0.02	9.55±0.02
Par-Lup3-4	...	21.19:	19.53±0.04	18.18±0.05	17.74±0.06	15.46±0.06	14.26±0.04	13.31±0.04
Sz110	15.27±0.05	14.58±0.05	13.72±0.05	12.28±0.01	12.09±0.02	10.97±0.02	10.22±0.02	9.75±0.02
Sz111	15.34±0.05	13.98±0.05	13.29±0.05	12.24±0.01	...	10.62±0.02	9.80±0.02	9.54±0.02
Sz112	16.62±0.05	15.39±0.05	14.92±0.01	12.93±0.01	12.12±0.01	11.00±0.02	10.29±0.02	9.96±0.02
Sz113	17.46±0.05	16.5 ±0.05	16.73±0.01	14.65±0.01	13.69±0.01	12.47±0.02	11.72±0.02	11.26±0.02
2MASS J16085953-3856275	19.79±0.04	16.91±0.02	15.56±0.02	13.90±0.03	13.29±0.03	12.84±0.03
SSTc2d160901.4-392512	16.92±0.05	15.31±0.05	15.23±0.01	13.49±0.01	13.23±0.01	11.61±0.02	10.68±0.02	10.29±0.02
Sz114	15.33±0.04	14.12:	14.73±0.01	12.54±0.01	11.58±0.01	10.41±0.02	9.70±0.02	9.32±0.02
Sz115	16.88±0.05	15.48±0.05	15.17±0.01	13.12±0.01	12.44±0.01	11.33±0.03	10.65±0.03	10.45±0.03
Lup818s	17.37±0.05	...	17.58±0.02	15.28±0.01	14.24±0.01	13.01±0.03	12.39±0.03	11.99±0.03
Sz123A (S)	16.27±0.05	14.90±0.05	15.04±0.01	13.37±0.01	12.68±0.01	11.47±0.02	10.55±0.02	10.03±0.02
Sz123B (N)	17.22±0.05	15.72±0.05	15.79±0.01	14.29±0.01	13.84±0.01	12.42±0.02	11.63±0.02	11.51±0.02
SST-Lup3-1	18.17±0.05	16.55±0.05	16.25±0.01	14.26±0.01	13.46±0.01	12.20±0.02	11.51±0.03	11.20±0.02

Table C.2. Available photometric fluxes, in milli Jy, from 3.4 μ m to 70.0 μ m

Object	3.4 μ m	3.6 μ m	4.5 μ m	4.6 μ m	5.8 μ m	8.0 μ m	12.8 μ m	22.4 μ m	24.0 μ m	70.0 μ m
Sz66	115.32 \pm 4.14	95.80 \pm 4.98	81.50 \pm 4.98	106.18 \pm 3.32	82.50 \pm 3.99	100.00 \pm 4.84	95.31 \pm 2.90	144.77 \pm 8.80	167.00 \pm 15.50	< 50.00
AKC2006-19	5.46 \pm 0.12	5.48 \pm 0.27	4.06 \pm 0.27	4.03 \pm 0.08	3.29 \pm 0.16	3.73 \pm 0.18	3.84 \pm 0.15	7.54 \pm 0.89	3.44 \pm 0.38	< 50.00
Sz69	131.07 \pm 2.66	111.00 \pm 5.84	120.00 \pm 5.84	127.54 \pm 2.11	94.60 \pm 4.59	83.00 \pm 4.12	79.43 \pm 1.17	144.91 \pm 3.07	100.00 \pm 9.72	154.00 \pm 20.10
Sz71	126.92 \pm 2.69	104.53 \pm 2.02	...	140.00	163.97 \pm 2.27	276.62 \pm 6.12	260.00	...
Sz72	101.09 \pm 2.14	92.31 \pm 1.79	...	150.00	130.72 \pm 1.69	232.86 \pm 3.86	250.00	...
Sz73	303.61 \pm 6.71	361.43 \pm 6.66	...	500.00	421.46 \pm 5.82	920.21 \pm 10.17	1200.00	...
Sz74	865.99 \pm 28.71	897.90 \pm 20.68	759.20 \pm 10.49	1386.40 \pm 16.60
Sz83	1260.99 \pm 60.39	1739.52 \pm 59.28	...	1500.00	2400.80 \pm 19.90	4465.67 \pm 41.13	3500.00	...
Sz84	42.10 \pm 0.89	42.00 \pm 0.04	29.00 \pm 0.04	32.30 \pm 0.63	20.10 \pm 0.03	12.00 \pm 0.03	6.95 \pm 0.21	24.54 \pm 1.20	20.90 \pm 0.41	244.00 \pm 73.20
Sz130	58.49 \pm 1.19	59.00 \pm 3.02	53.50 \pm 3.02	51.91 \pm 0.91	53.30 \pm 2.53	70.10 \pm 3.35	79.21 \pm 1.17	133.63 \pm 2.71	115.00 \pm 10.60	165.00 \pm 22.10
Sz88A (SW)	< 292.90	< 264.99	< 300.85	< 363.99
Sz88B (NE)	< 292.90	< 264.99	< 300.85	< 363.99
Sz91	41.37 \pm 0.80	38.60 \pm 1.93	24.70 \pm 1.93	25.64 \pm 0.47	17.20 \pm 0.83	10.90 \pm 0.52	6.89 \pm 0.19	13.02 \pm 1.00	9.72 \pm 0.98	502.00 \pm 53.20
Lup713	6.72 \pm 0.15	6.96 \pm 0.46	6.12 \pm 0.46	6.12 \pm 0.13	5.65 \pm 0.31	6.69 \pm 0.33	5.62 \pm 0.26	5.36 \pm 1.16	6.39 \pm 0.64	< 50.00
Lup604s	16.49 \pm 0.35	16.30 \pm 0.90	15.10 \pm 0.90	13.72 \pm 0.25	12.80 \pm 0.64	14.40 \pm 0.69	14.02 \pm 0.30	21.22 \pm 1.15	16.60 \pm 1.57	< 50.00
Sz97	33.17 \pm 0.70	27.90 \pm 1.73	25.20 \pm 1.73	26.82 \pm 0.49	23.70 \pm 1.14	25.70 \pm 1.23	24.01 \pm 0.55	39.51 \pm 2.26	31.20 \pm 2.97	88.60 \pm 16.90
Sz99	25.70 \pm 0.54	23.80 \pm 1.39	22.90 \pm 1.39	22.22 \pm 0.41	20.10 \pm 1.01	21.10 \pm 1.00	24.41 \pm 0.52	30.33 \pm 1.65	26.20 \pm 2.45	< 50.00
Sz100	59.58 \pm 1.32	53.10 \pm 3.21	50.40 \pm 3.21	51.86 \pm 1.00	48.70 \pm 2.48	61.70 \pm 3.04	67.98 \pm 1.13	140.44 \pm 3.62	130.00 \pm 12.10	223.00 \pm 28.50
Sz103	40.28 \pm 0.93	32.10 \pm 1.97	28.10 \pm 1.97	33.89 \pm 0.69	30.00 \pm 1.81	33.80 \pm 1.77	39.77 \pm 1.21	151.04 \pm 4.31	81.20 \pm 7.66	317.00 \pm 40.00
Sz104	...	25.50 \pm 1.47	22.50 \pm 1.47	...	20.00 \pm 1.01	21.30 \pm 1.10	47.90 \pm 4.62	441.00 \pm 53.20
Lup706	...	2.23 \pm 0.15	2.01 \pm 0.15	...	1.77 \pm 0.11	1.93 \pm 0.11	1.29 \pm 0.54	< 50.00
Sz106	67.53 \pm 1.49	60.10 \pm 4.42	81.30 \pm 4.42	60.65 \pm 1.12	72.10 \pm 3.58	73.80 \pm 3.86	54.90 \pm 1.01	106.83 \pm 2.66	69.50 \pm 6.56	< 50.00
Par-Lup3-3	65.63 \pm 1.45	69.40 \pm 4.79	79.00 \pm 4.79	64.63 \pm 1.19	77.60 \pm 3.75	127.00 \pm 6.39	162.46 \pm 2.84	301.08 \pm 6.66	191.00 \pm 18.10	< 50.00
Par-Lup3-4	2.77 \pm 0.07	2.80 \pm 0.15	2.88 \pm 0.15	3.39 \pm 0.08	2.24 \pm 0.13	1.73 \pm 0.10	10.40 \pm 0.47	69.93 \pm 2.83	26.60 \pm 2.55	492.00 \pm 53.60
Sz110	70.85 \pm 1.44	69.90 \pm 3.61	67.80 \pm 3.61	63.51 \pm 1.17	58.80 \pm 2.82	70.50 \pm 3.45	99.62 \pm 1.56	193.33 \pm 4.27	171.00 \pm 16.20	< 50.00
Sz111	50.76 \pm 1.08	31.48 \pm 0.55	8.47 \pm 0.26	42.18 \pm 1.40	41.50 \pm 3.86	< 50.00
Sz112	49.42 \pm 1.14	48.70 \pm 2.96	38.00 \pm 2.96	39.38 \pm 0.69	30.40 \pm 1.49	24.80 \pm 1.22	38.33 \pm 0.64	152.72 \pm 3.66	124.00 \pm 11.70	120.00 \pm 25.20
Sz113	25.09 \pm 0.56	15.40 \pm 0.89	15.00 \pm 0.89	26.16 \pm 0.43	14.90 \pm 0.72	20.50 \pm 0.99	32.39 \pm 0.51	59.69 \pm 1.76	56.10 \pm 5.35	88.30 \pm 16.00
2MASS J16085953-3856275	3.42 \pm 0.07	3.89 \pm 0.21	3.69 \pm 0.21	3.66 \pm 0.07	3.77 \pm 0.23	4.31 \pm 0.21	4.94 \pm 0.18	8.37 \pm 0.95	5.40 \pm 0.57	< 50.00
SSTc2d160901.4-392512	43.48 \pm 0.84	44.70 \pm 2.95	34.00 \pm 2.95	33.73 \pm 0.62	30.60 \pm 1.61	25.80 \pm 1.29	23.40 \pm 0.45	58.98 \pm 2.23	42.20 \pm 3.96	114.00 \pm 15.00
Sz114	118.34 \pm 2.51	95.70 \pm 5.43	101.00 \pm 5.43	124.17 \pm 2.40	97.20 \pm 4.66	121.00 \pm 6.02	170.28 \pm 2.35	374.53 \pm 8.28	347.00 \pm 32.30	257.00 \pm 30.50
Sz115	25.94 \pm 0.55	22.20 \pm 1.36	18.40 \pm 1.36	18.79 \pm 0.38	14.80 \pm 0.72	12.40 \pm 0.59	10.59 \pm 0.51	12.53 \pm 1.66	10.50 \pm 1.01	< 50.00
Lup818s	7.42 \pm 0.26	7.44 \pm 0.39	6.50 \pm 0.39	7.17 \pm 0.20	5.81 \pm 0.29	7.63 \pm 0.37	7.52 \pm 0.21	12.45 \pm 1.01	11.70 \pm 1.12	96.90 \pm 22.10
Sz123A (S)	< 55.20	< 59.90	< 50.40	< 45.97	< 42.60	< 44.90	< 43.65	< 72.36	< 61.00	< 327.00
Sz123B (N)	< 55.20	< 59.90	< 50.40	< 45.97	< 42.60	< 44.90	< 43.65	< 72.36	< 61.00	< 327.00
SST-Lup3-1	14.02 \pm 0.30	15.80 \pm 0.84	13.10 \pm 0.84	11.48 \pm 0.21	11.00 \pm 0.53	12.90 \pm 0.61	13.27 \pm 0.31	20.70 \pm 1.64	21.00 \pm 1.98	< 50.00

Notes:

- fluxes at 3.4 μ m, 4.6 μ m, 12.8 μ m and 22.4 μ m are from the WISE catalog, while those at 3.6 μ m, 4.5 μ m, 5.8 μ m, 8.0 μ m, 24.0 μ m and 70.0 μ m are from Spitzer surveys.
- the components of Sz88 and Sz123 are not resolved in the mid-IR images. Thus, their fluxes are given as upper limits.
- Spitzer fluxes marked with “:” were estimated from Spitzer spectra (Olofsson et al. 2010)
- the only YSO in our sample with 160 μ m data available is Sz111 with a flux of 1678.00 \pm 335.60 mJy.

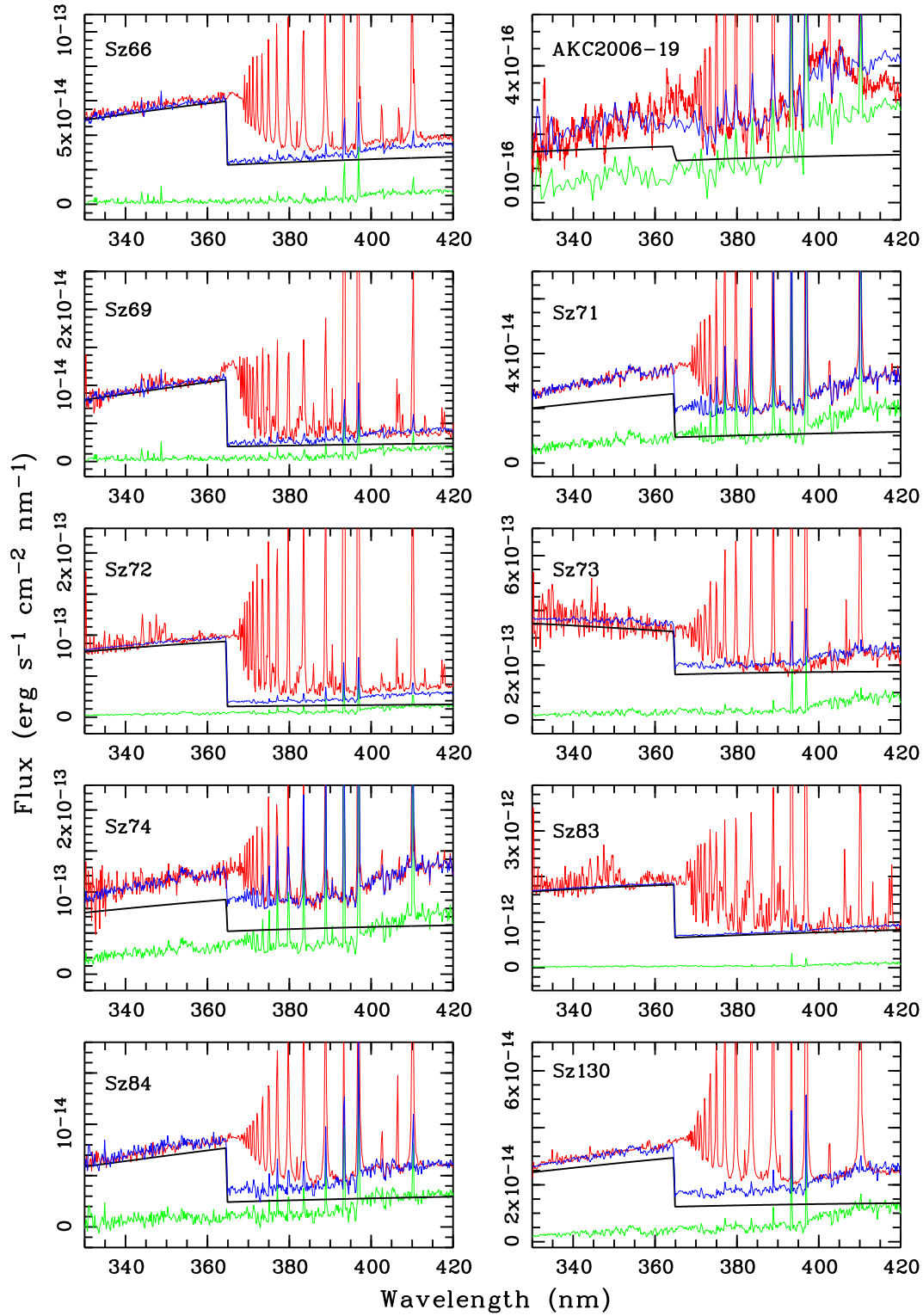


Fig. C.1. Extinction corrected spectra (red) fitted with a combination of a photospheric template (green) and the synthetic continuum spectrum from a hydrogen slab (black). The total fit is represented with the blue line.

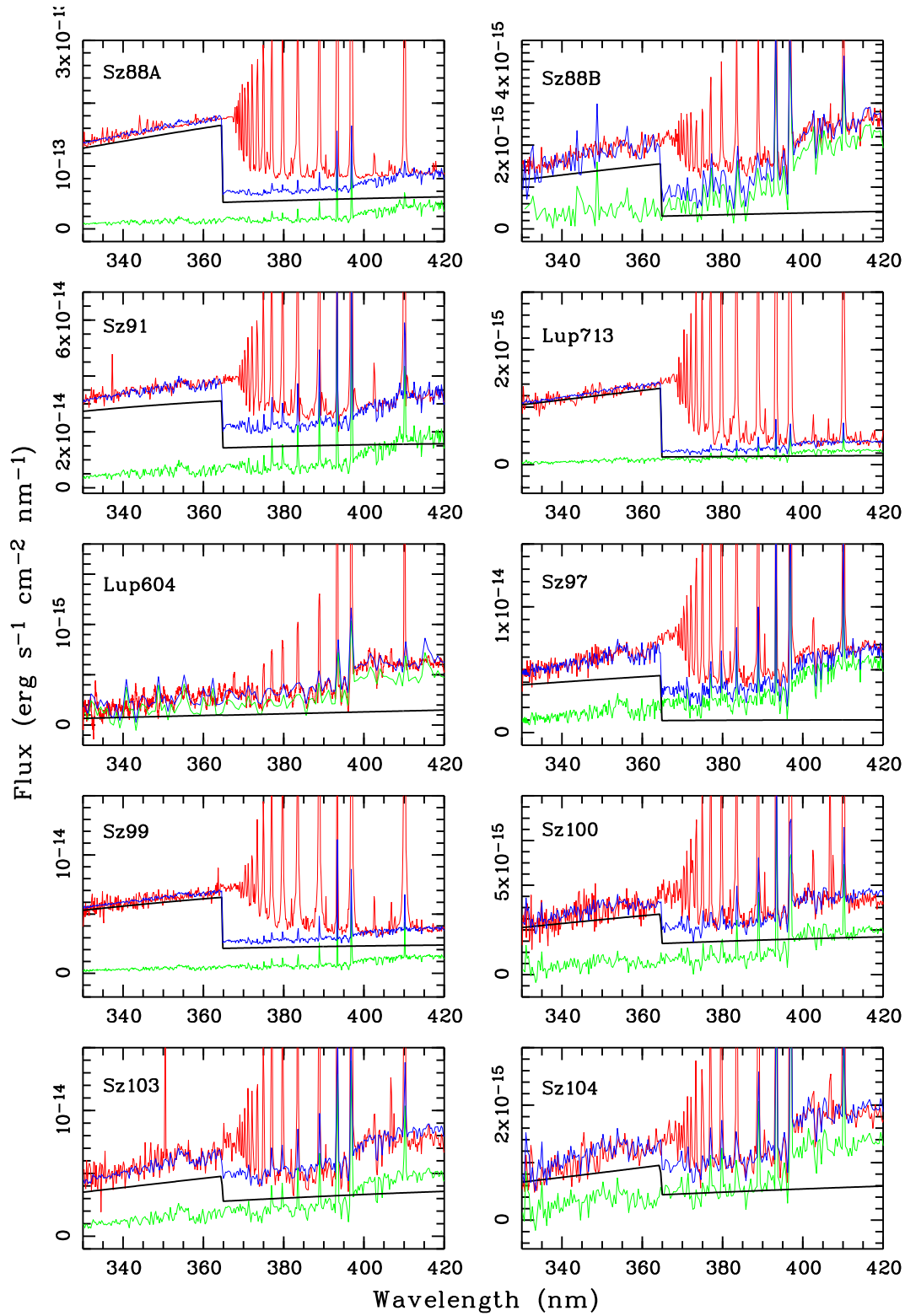


Fig. C.2. Extinction corrected spectra (red) fitted with a combination of a photospheric template (green) and the synthetic continuum spectrum from a hydrogen slab (black). The total fit is represented with the blue line.

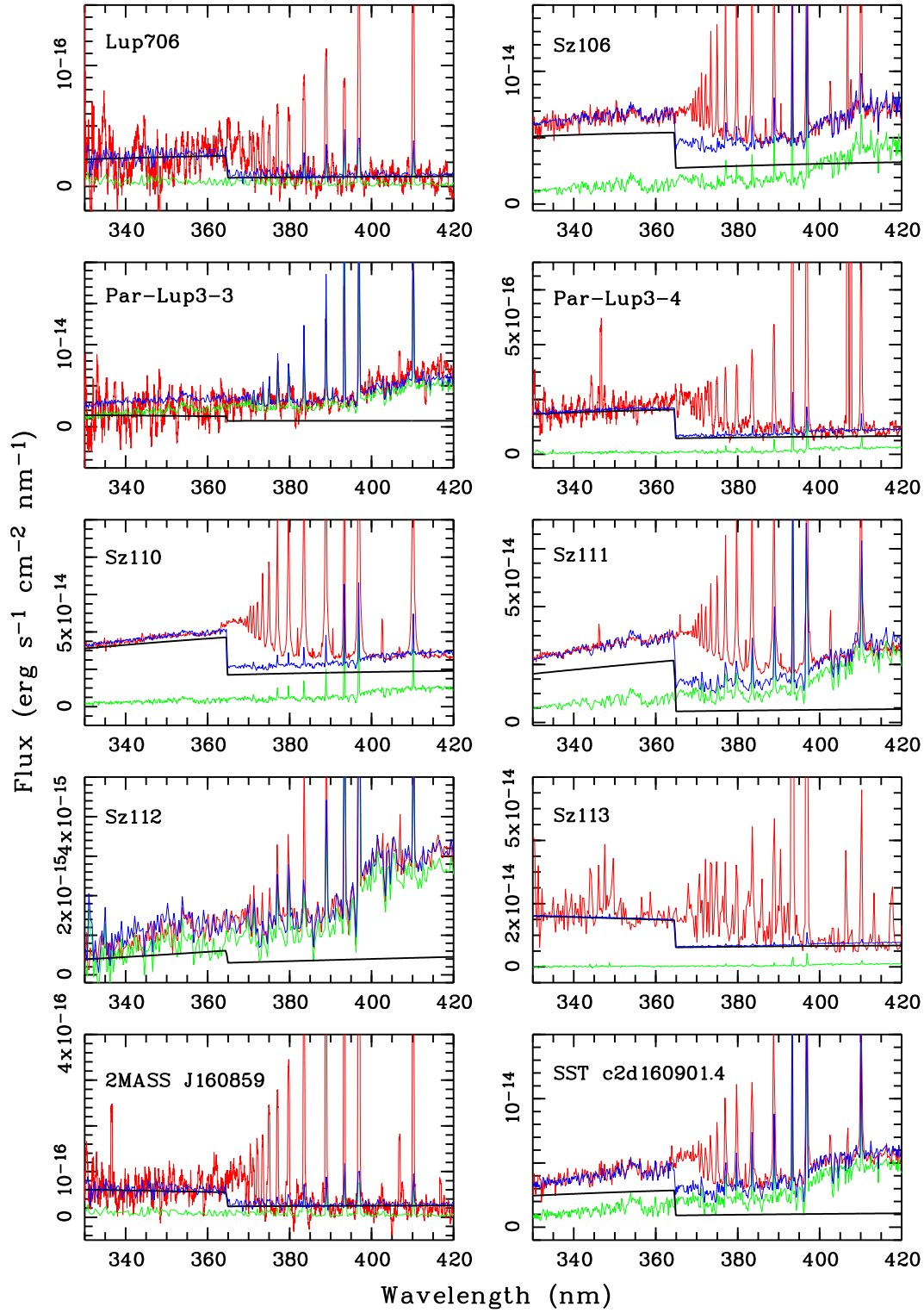


Fig. C.3. Extinction corrected spectra (red) fitted with a combination of a photospheric template (green) and the synthetic continuum spectrum from a hydrogen slab (black). The total fit is represented with the blue line.

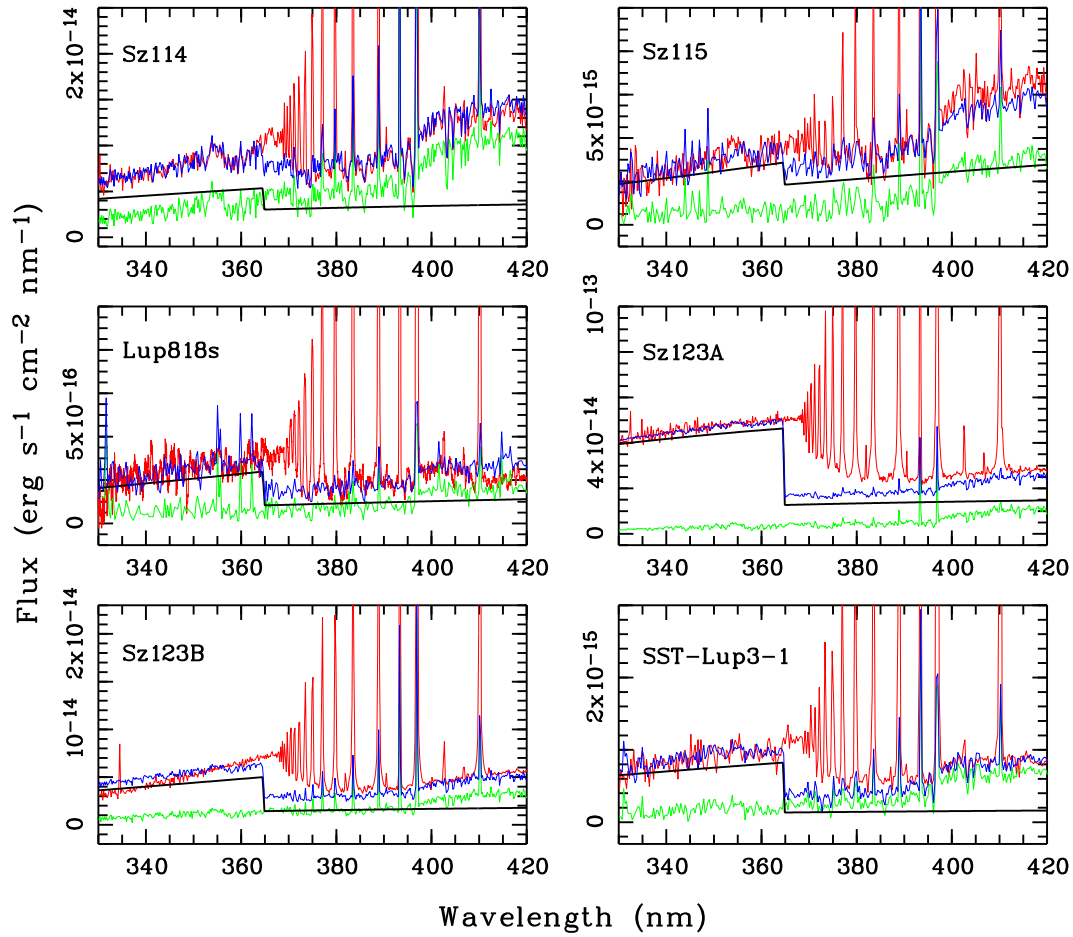


Fig. C.4. Extinction corrected spectra (red) fitted with a combination of a photospheric template (green) and the synthetic continuum spectrum from a hydrogen slab (black). The total fit is represented with the blue line.

Table C.11. Extinction corrected fluxes and equivalent widths of the Na I D lines

Object	$f_{\text{Na I } \lambda 588.99}$ ($\text{erg s}^{-1} \text{cm}^{-2}$)	$EW_{\text{Na I } \lambda 588.99}$ (nm)	$f_{\text{Na I } \lambda 589.59}$ ($\text{erg s}^{-1} \text{cm}^{-2}$)	$EW_{\text{Na I } \lambda 589.59}$ (nm)

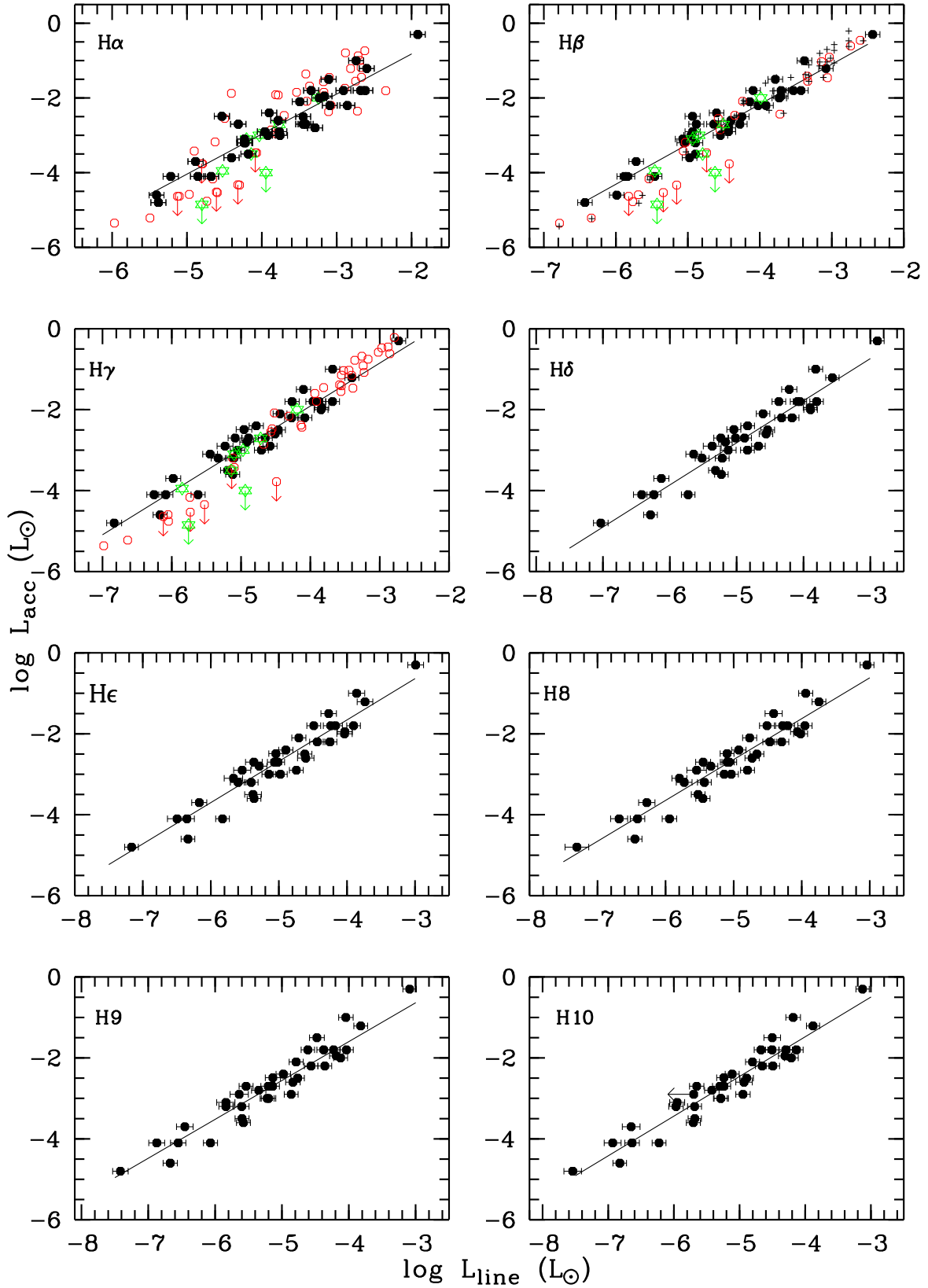


Fig. C.5. Relationships between accretion luminosity and line luminosity for the several diagnostics as labelled in each panel. The Lupus YSOs are represented with black dots. The $H\alpha$, $H\beta$ and $H\gamma$ data available in literature for YSOs in Taurus (Herczeg & Hillenbrand 2008), and the σ -Ori cluster (Rigliaco et al. 2012), are overlaid with open circles and star symbols, respectively.

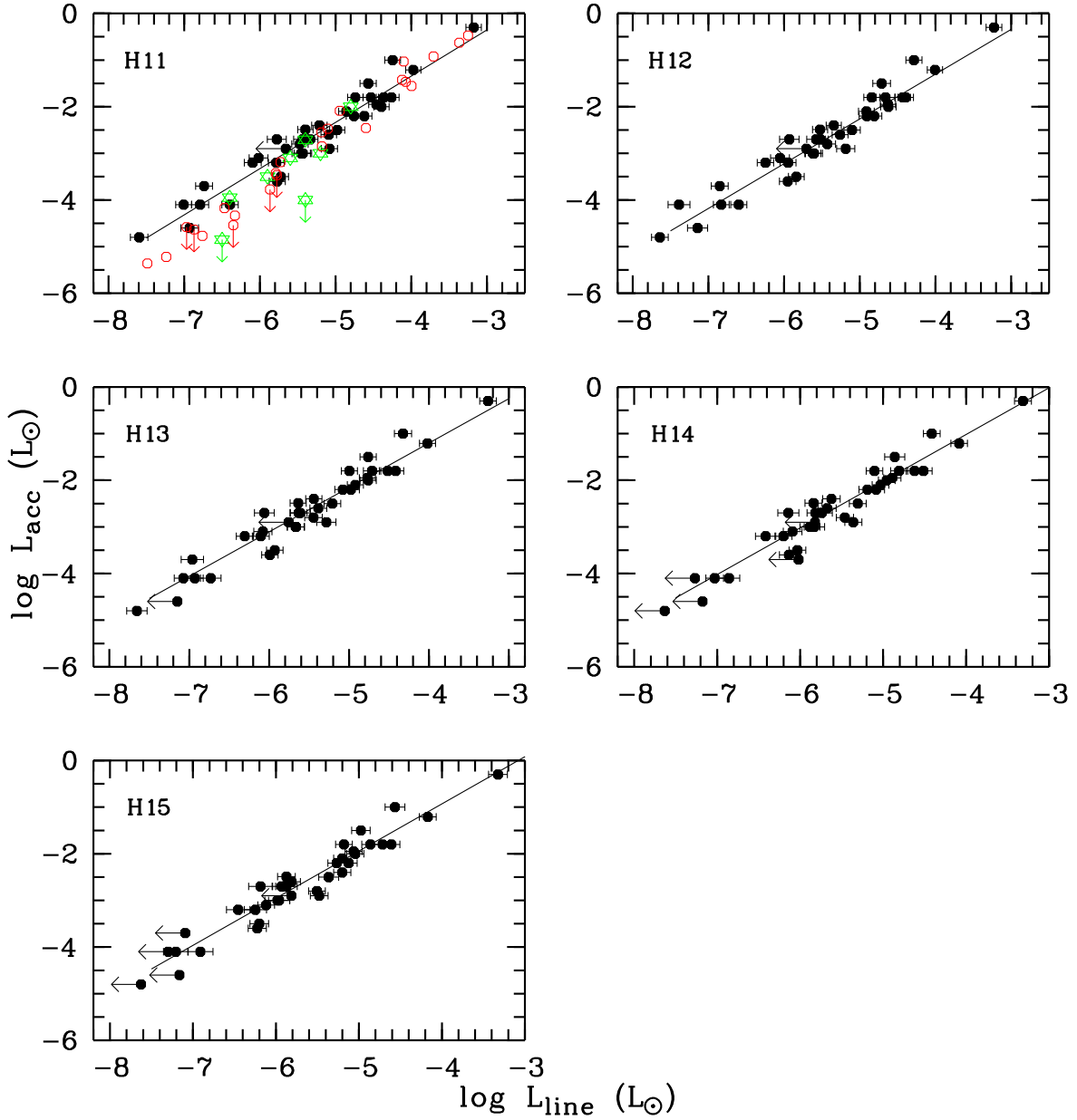


Fig. C.6. Relationships between accretion luminosity and line luminosity for the several diagnostics as labelled in each panel. The Lupus YSOs are represented with black dots. The H11 data available in literature for YSOs in Taurus (Herczeg & Hillenbrand 2008) and the σ -Ori cluster (Rigliaco et al. 2012), are overlaid with open circles and star symbols, respectively.

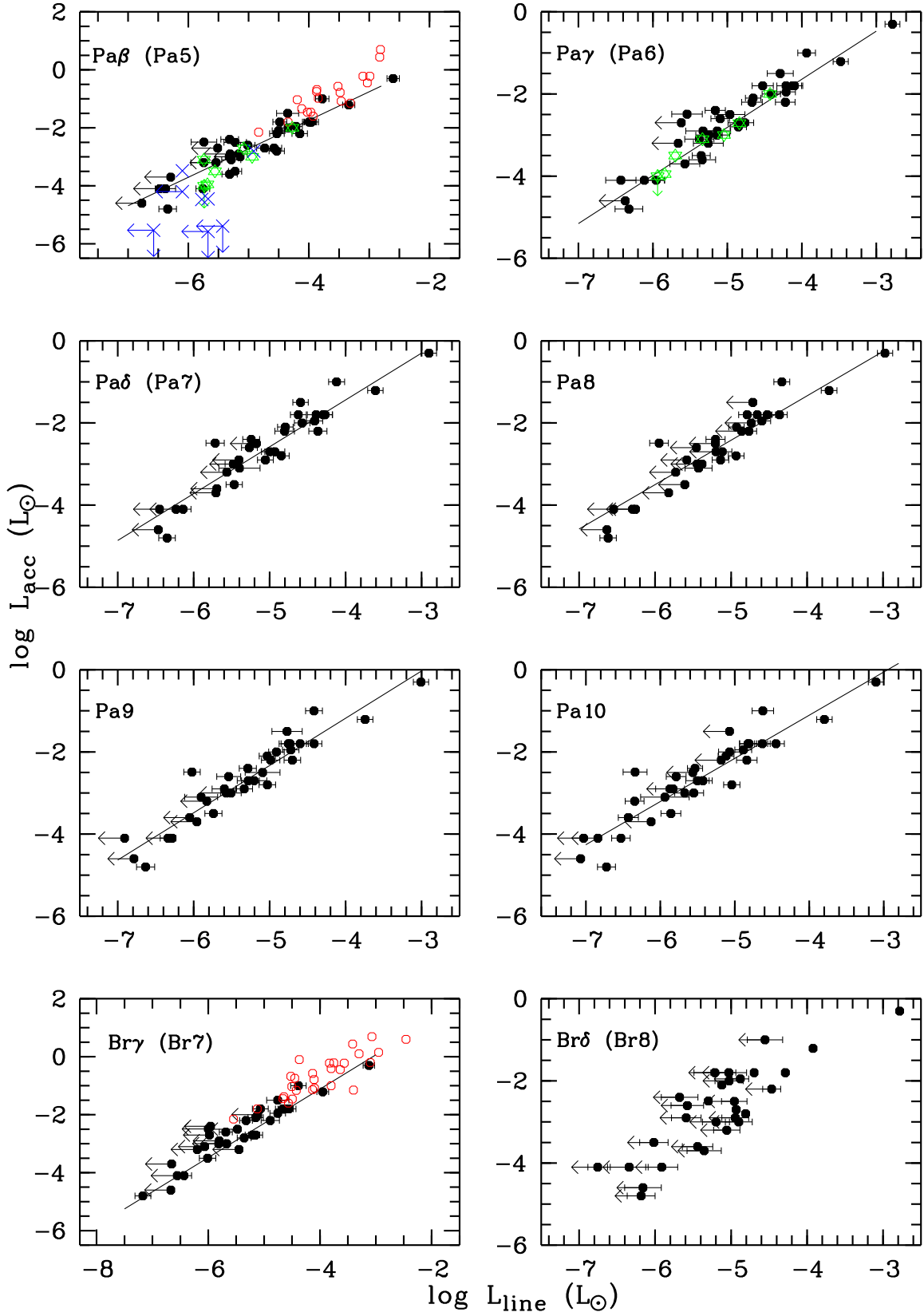


Fig. C.7. Relationships between accretion luminosity and line luminosity for the several diagnostics as labelled in each panel. The Lupus YSOs are represented with black dots. The $\text{Pa}\beta$, $\text{Pa}\gamma$ and $\text{Br}\gamma$ data available in literature for YSOs in Taurus (Muzerolle et al. 1998; Calvet et al. 2000, 2004), ρ -Oph and Chamaeleon (Natta et al. 2004) and the σ -Ori cluster (Rigliaco et al. 2012), are overlaid with open circles, \times -symbols and star symbols, respectively.

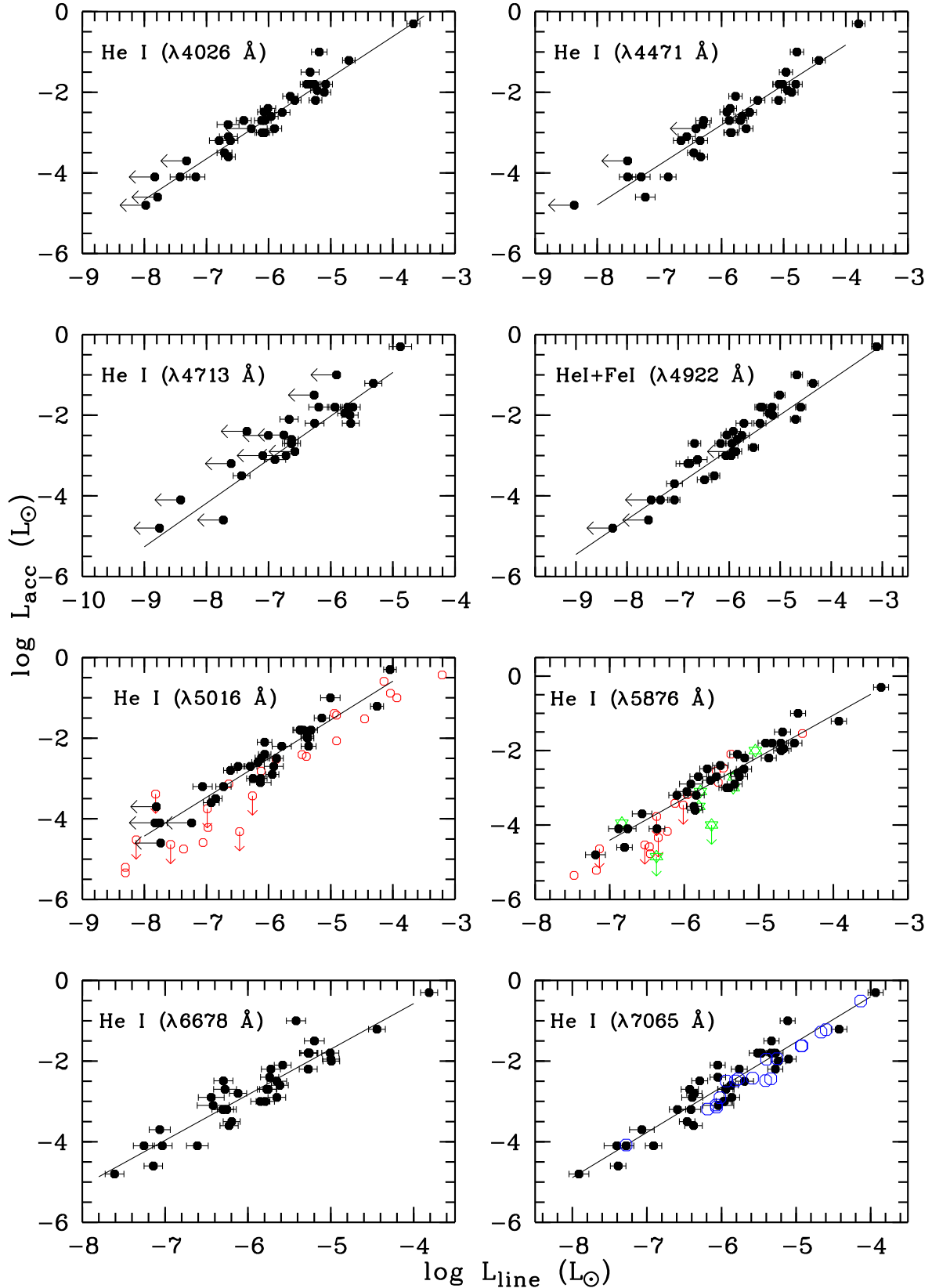


Fig. C.8. Relationships between accretion luminosity and line luminosity for the several diagnostics as labelled in each panel. The Lupus YSOs are represented with black dots. The He I ($\lambda 5016 \text{ \AA}$), He I ($\lambda 5876 \text{ \AA}$), and He I ($\lambda 7065 \text{ \AA}$) data available in literature for YSOs in Taurus (Herczeg & Hillenbrand 2008), the σ -Ori cluster (Rigliaco et al. 2012), and the Cha-II cloud (Biazzo et al. 2012), are overlaid with small open circles, star symbols and big open circles, respectively.

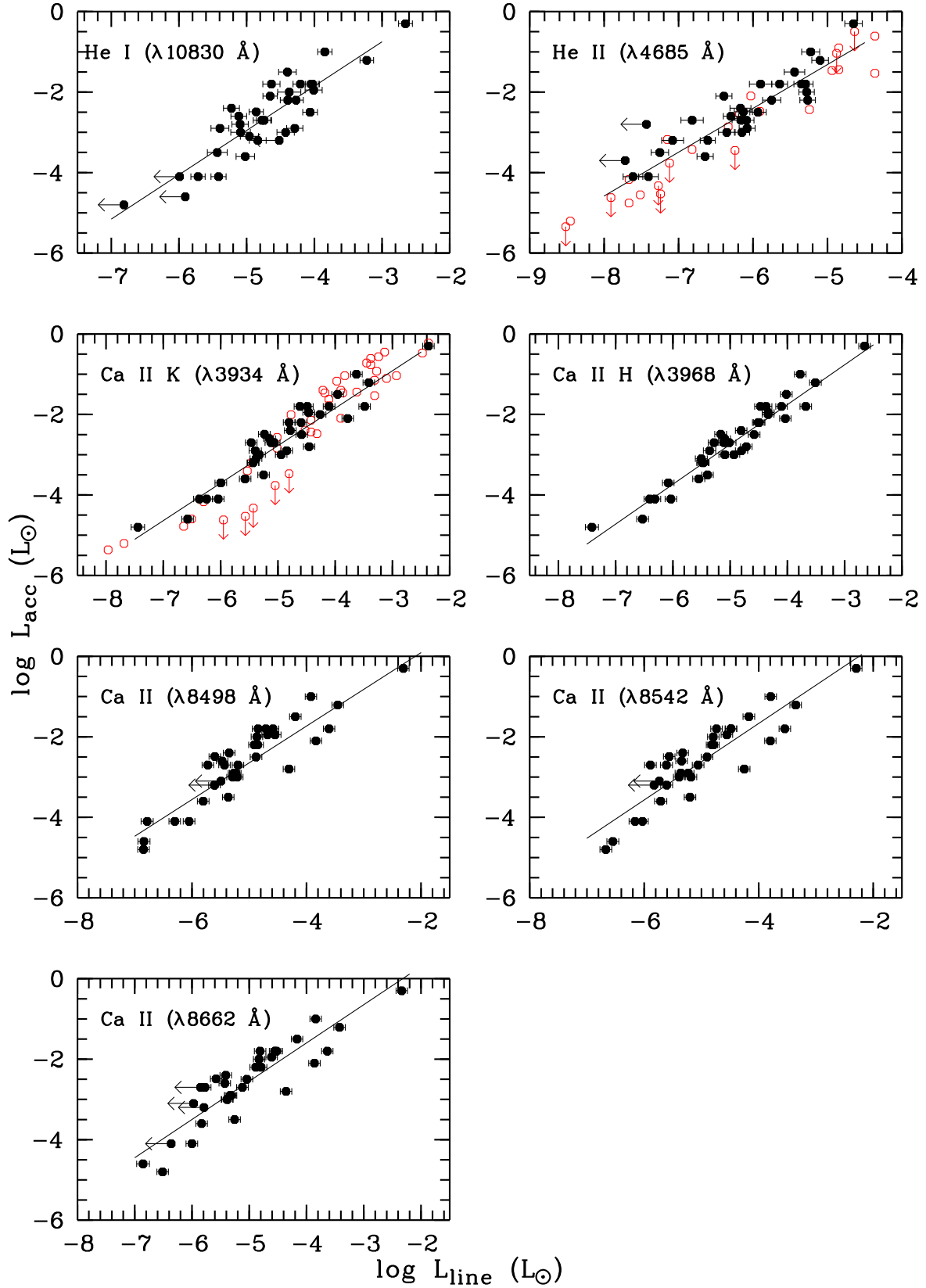


Fig. C.9. Relationships between accretion luminosity and line luminosity for the several diagnostics as labelled in each panel. The Lupus YSOs are represented with black dots. The He II ($\lambda 4685 \text{ \AA}$) and Ca II K data available in literature for YSOs in Taurus (Herczeg & Hillenbrand 2008) are overlaid with open circles.

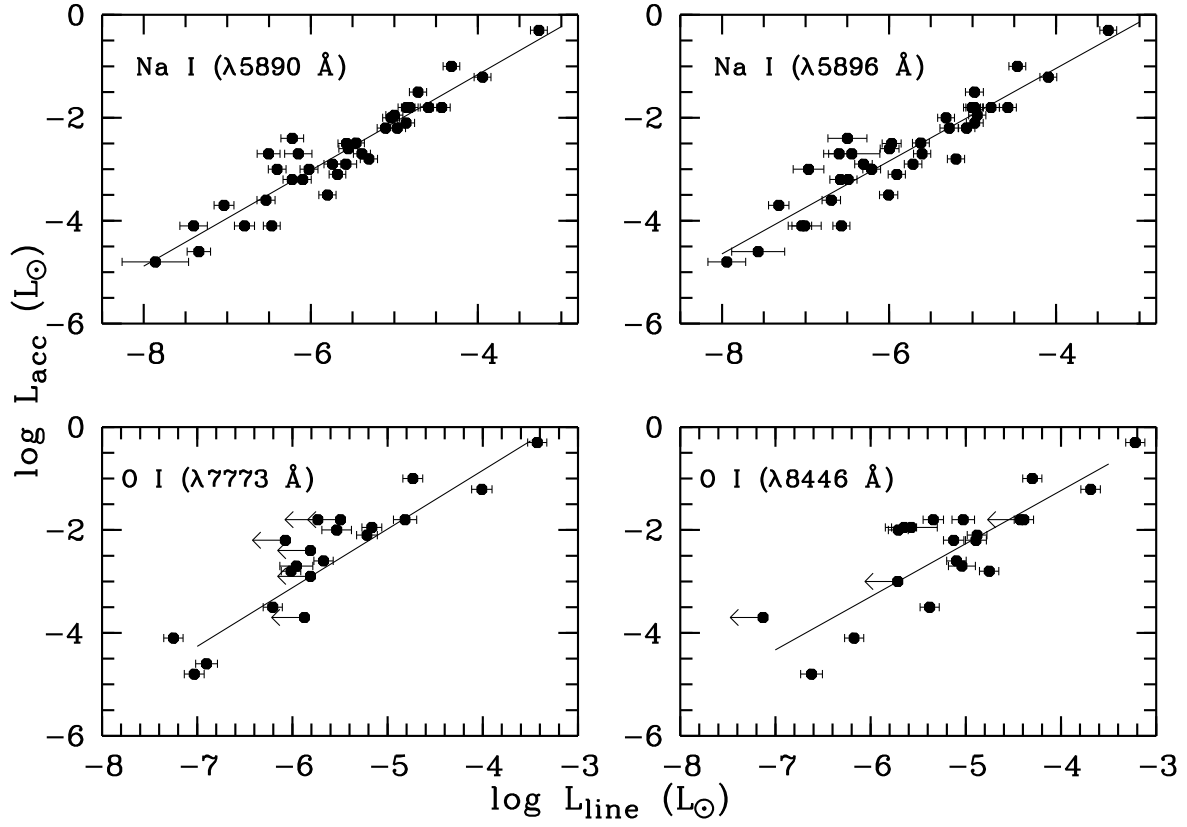


Fig. C.10. Relationships between accretion luminosity and line luminosity for the several diagnostics as labelled in each panel. The Lupus YSOs are represented with black dots.